

1 **Significant Local wind disturbances regime induced**  
2 **by the presence of giant linear dunes.**

3 Cyril Gadal · Pauline Delorme ·  
4 Clément Narteau · Giles F.S. Wiggs ·  
5 Matthew Baddock · Joanna M. Nield ·  
6 Philippe Claudin

7  
8 Received: DD Month YEAR / Accepted: DD Month YEAR

9 **Abstract**

10 ~~abstract~~ In large-scale studies of arid areas, sediment fluxes and resulting  
11 geomorphological quantities (sediment pathways, erosion rates, dune morphodynamics)  
12 are often derived from wind data. However, the feedback of nearby topography  
13 on the flow, such as kilometric giant dunes, is rarely taken into account  
14 because barely studied. Here, we compare locally measured wind data to  
15 the predictions of the Era5Land climate reanalysis in four different places  
16 across and around the Namib sand sea. In places with flat environments, we  
17 show that the two wind datasets agree with each other. In contrast, within  
18 the sand sea, we show that they significantly differ due to the presence of  
19 giant linear dunes. We quantify this discrepancy, and link it to dynamics of  
20 the atmospheric boundary layer. Aside setting limits to the applicability of  
21 the Era5land dataset, this study highlights the giant dunes feedback on the  
22 wind, and discuss its implications for smaller scale bedforms. All codes used,  
23 from the raw data to the figures of the paper, are publicly available with  
24 full documentation at <https://github.com/Cgadal/GiantDunes> (will be made  
25 public upon acceptance of this manuscript for publication).

26 **Keywords** Boundary layer · Turbulent flow · Sand dunes · Fluid-structures  
27 interactions

---

C. Gadal

Institut de Mécanique des Fluides de Toulouse (IMFT), Université de Toulouse, CNRS,  
INPT, UPS, Toulouse, France  
E-mail: [cyril.gadal@imft.fr](mailto:cyril.gadal@imft.fr)

S. Author  
second address

T. Author  
third address

## 28 1 Introduction

29 Whenever ~~As~~ a flow encounters an obstacle, different interactions can arise de-  
 30 pending on the different time and length scales involved. In the case of atmo-  
 31 spheric flows, this mainly depends on the part of the atmosphere, schematically  
 32 composed of a turbulent boundary layer topped by a ~~part free of turbulence~~stable  
 33 ~~stratified one~~, with which the obstacle interacts (Stull 1988). At the largest  
 34 scale, the feedback of mountains on the stratified ~~flow of the~~ free atmosphere re-  
 35 sults in wave generation as well as significant wind disturbances, such as down-  
 36 slope winds in the lee side (Durran 1990). Inside the boundary layer, the interac-  
 37 tion between a turbulent flow and hilly surfaces is for example key to the under-  
 38 standing ocean surface wind-driven waves (Sullivan and McWilliams 2010), or  
 39 eolian bedforms in desert (~~?Sullivan and McWilliams 2010; Courrech du Pont 2015~~)  
 40 (~~Courrech du Pont 2015~~).

41 ~~Indeed, eolian sand dunes typically emerge from the feedback Looking at~~

42 ~~the flow close to the surface, two different components~~ of the topography ~~on the~~

43 ~~turbulent flow, which speeds up close to the dune crest (Rubin and Hunter 1987; ?; Courrech du Pont et al. 2014)~~

44 ~~. Later on, when the dune reaches an intermediate size, it may also induce~~

45 ~~significant wind deflections. For exemple, this can affect feedback can be~~

46 ~~isolated. First, the flow accelerates on the upwind slope, and slows down on the~~

47 ~~downwind one, with a maximum velocity slightly upwind of the crest (Jackson and Hunt 1975; Sykes 1980; Hunt et al. 198~~

48 ~~. Several measurements are available, performed in subaqueous flumes (Zilker et al. 1977; Zilker and Hanratty 1979; Freder~~

49 ~~and in eolian field conditions (Claudin et al. 2013; Lü et al. 2021). Second,~~

50 ~~deflection occurs when the incident flow direction is not perpendicular to~~

51 ~~the ridge crest. While predicted to be small (less than 10°) in the linear~~

52 ~~regime (Gadal et al. 2019), significant flow steering has been reported in the~~

53 ~~field on the downwind side of larger aspect ratios obstacles, such as mountain~~

54 ~~ranges (Kim et al. 2000; Lewis et al. 2008; Fernando et al. 2019) or sand dunes (Walker et al. 2009; Walker and Shugar 2~~

55 ~~~~~

56 ~~In the case of aeolian bedforms, the measurements mentioned above were~~

57 ~~made on dunes a few meters high only. The resulting wind disturbances have~~

58 ~~then been shown to significantly impact the sediment pathways of coastal~~

59 ~~systems (Hesp et al. 2015), or the collective behavior the whole system (Hesp et al. 2015)~~

60 ~~, but also to affect the collective behaviour of dune populations ,through~~

61 ~~trough long-range interactions due to flow disturbances induced by each individual~~

62 ~~(Smith et al. 2017; Bacik et al. 2020). As the dunes increase in size by collisions~~

63 ~~and coarsening, they sometimes reach a giant sizecomparable to the boundary~~

64 ~~layer depth (Andreotti et al. 2009). However, the (Bacik et al. 2020). However,~~

65 ~~eolian dunes coexists in sand seas at different scales, each representative of~~

66 ~~their different evolution stages, from emergence at twenty meters wavelengths~~

67 ~~to giant size, corresponding to kilometric wavelengths and heights of several~~

68 ~~dozen meters (McKee 1979). Quantifying these two effects for giant dunes is~~

69 ~~then all the more important for several reasons. First, larger wind disturbances~~

70 ~~are expected from larger obstacles. Second, the flow structure coupling is not~~

71 ~~straightforward due to vertical structure of the atmosphere with which the~~

72 ~~giant dunes interact due to their sizes (Andreotti et al. 2009). Finally, the~~

73 morphodynamics of aeolian bedforms are strongly dependent on the wind  
74 regime (Livingstone and Warren 1996). Thus, small-scale bedforms are sensitive  
75 to wind disturbances induced by these giant dunes have never been quantified larger-scale  
76 bedforms. This has been demonstrated for impact ripples on dunes (Howard 1977; Hood et al. 2021)  
77 , but has never been studied for medium-scale dunes near giant dunes.

78 The study of the feedback of obstacles on atmospheric flows allows its  
79 incorporation into numerical meteorological models . The latter then become  
80 mainly limited by the accuracy of the included topographical data, as well as  
81 by the spatial grid of the model. For example, the In the literature, arid areas  
82 have been studied at the desert scale from climate reanalyses based on global  
83 atmospheric models (Blumberg and Greeley 1996; Livingstone et al. 2010; Ashkenazy et al. 2012; Jolivet et al. 2021; Hu  
84 , such as ERA-40, ERA-Interim or ERA-5 (Uppala et al. 2005; Dee et al. 2011; Hersbach et al. 2020)  
85 . However, the spatial resolution (tens of kilometers) of these reanalyses implies  
86 average quantities that do not resolve the smaller scales, ranging from the  
87 study of individual dunes to the border of mountains (Livingstone et al. 2010)  
88 . Lately, the release of ERA5-Land climate reanalysis is limited by its 9 km  
89 spatial resolution , while including the data 30-m Digital Elevation Models  
90 (DEMs) of the shuttle radar topography mission (Farr et al. 2007; Muñoz-Sabater et al. 2021)  
91 . As such, it can not reproduce the flow disturbances induced by giant dunes,  
92 which have a typical length scale ~ 1 km allow to push back this limitation  
93 by providing up to 70 years of hourly wind predictions at a 9 km spatial  
94 resolution (Muñoz-Sabater et al. 2021). However, due to its recent nature, the  
95 applicability limitations of this dataset remain to be studied.

96 Here, we compare the wind speed and direction of the ERA5-Land dataset  
97 to local measurements local wind speeds and directions measured in four differ-  
98 ent places across the Namib desert .Where no significant topographies smaller  
99 than the model grid are present to the regional predictions of the ERA5-Land  
100 climate reanalysis. When the measurement stations are surrounded by a relatively  
101 flat environment, we show that the two wind datasets local measurements  
102 and regional predictions agree with each other. On the contrary, in placees  
103 with giant dunes the sand sea, we show that they may differ for some specific  
104 meteorological conditions, that we link differ due to the presence of giant  
105 dunes. Furthermore, we link the magnitude of these discrepancies to the cir-  
106 cadian cycle of the atmospheric boundary layer. In doing so, we highlight the  
107 importance of medium scale topographies for local wind regimes and, in the  
108 ease of sand seas, Finally, we draw implications for smaller-scale eolian bed-  
109 forms.

## 110 2 Wind regimes across the Namib Sand Sea

111 In this study, we We focus on four places across and nearby the Namib desert,  
112 highlighting different environments (see Fig. 1). The Adamax station is lo-  
113 cated near the Adamax salt pan, in a highly vegetated area. The Huab sta-  
114 tion, located on the coast at the outlet of the Huab riveris , is in an arid  
115 environment exhibiting 60-m scale barchan dunes. While the surroundings of

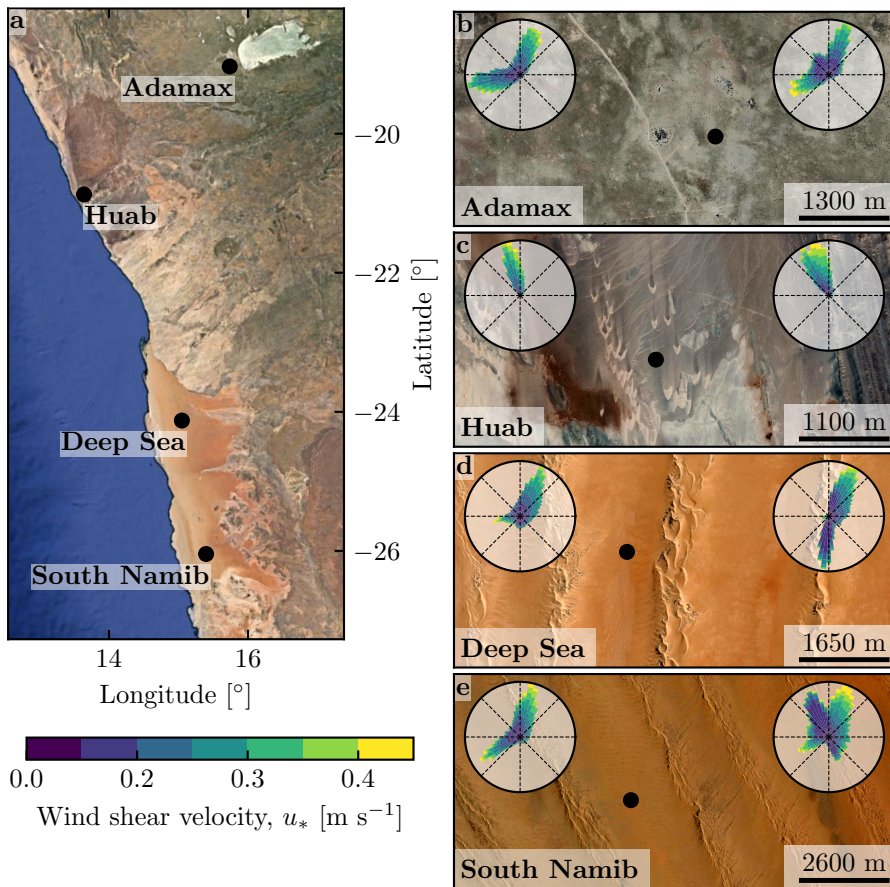


**Fig. 1** Wind data used in this study **a**: Location of the studied sites. **b–e**: Satellite images of the studied sites (Google-Earth, Maxar Technologies, CNES/Airbus). In each subplot, the left and right wind roses represent the data from the ERA5Land climate reanalysis and the local wind stations, respectively. Note that the bars show the direction towards which the wind blows. The red black dots show the location of local wind stations.

116 these two stations are in environments with no mid-scale topography relatively  
 117 flat, this is not the case for the Deep Sea and South Namib stations. Both are  
 118 located in the interdune between tens of meters high giant linear dunes with  
 119 kilometric wavelengths and superimposed patterns. In this section, we describe  
 120 and compare the wind regimes resulting from the available datasets in each  
 121 station winds from local measurements and climate reanalysis predictions.

## 122 2.1 Datasets

123 Two wind datasets are used in this study. First, local Local winds are provided  
 124 by stations situated measurement stations located in the four different places

(see black dots in Fig. 1). The wind strength and direction are ~~measured~~  
~~sampled~~ every 10 minutes by cup anemometers and wind vanes, at heights  
between 2 m and 3 m depending on the station. The available period of mea-  
surements ranges from 1 to 5 discontinuous years distributed between 2012  
and 2020 (see Fig. S1). We checked that at least one complete seasonal cy-  
cle is available at each station. ~~Then, regional~~ Regional winds are extracted  
at the same locations and periods from the ERA5-Land dataset, which is a  
replay at a smaller spatial resolution of ERA5, the latest climate reanalysis  
from the ECMWF (Hersbach et al. 2020; Muñoz-Sabater et al. 2021). It  
provides hourly ~~estimates~~ predictions of the 10-m wind velocity and direction  
at a spatial resolution of  $\sim 9$  km ( $0.1^\circ \times 0.1^\circ$ ).

For comparison, the local measurements are averaged into 1-hr bins cen-  
tered on the temporal scale of the ERA5-Land estimates (see Fig. S2). As the  
wind velocities of both datasets are provided at different heights, we convert  
them into shear velocities (see SI section 1), characteristic of the ~~whole~~ turbu-  
lent wind profile ~~within the atmospheric boundary layer~~, which are then used  
together with the wind direction for further analysis. The resulting wind data  
are shown on the wind roses of Fig. 1(b-e).

Finally, the dune properties are computed using autocorrelation on the 30-  
m Digital Elevation Models (DEMs) of the shuttle radar topography mission  
(Farr et al. 2007). For the South Namib and Deep Sea stations, we obtain  
respectively orientations of  $85^\circ$  and  $125^\circ$ , wavelengths of 2.6 km and 2.3 km  
and amplitudes of 45 m and 20 m (see Fig. S4 for more details).

## 2.2 Agreement between local and regional winds

The obtained wind regimes are shown in figure 1. In the Namib, the regional  
wind patterns are essentially controlled by the sea breeze, resulting in strong  
northward components (sometimes slightly deviated by the large scale topog-  
raphy) present in all regional wind roses (Lancaster 1985). These ~~daily~~ daytime  
winds are dominant during the second-half of the year (Septembre-January).  
In winter, an additional easterly component can be recorded during the night,  
induced by the combination of katabatic winds forming on the mountains,  
and infrequent ‘berg’ winds, which are responsible of the high wind velocities  
observed (Lancaster 1984). The frequency of these easterly components de-  
creases from the inland to the coast, resulting in bidirectional wind regimes  
within the Namib Sand Sea and at the Adamax salt pan (Fig. 1b, 1d and 1e)  
and a unidirectional wind regime on the coast at the outlet of the Huab River  
(Fig. 1c).

In the case of the Adamax and Huab stations, the ~~regional wind roses~~ wind  
roses from the regional predictions qualitatively match those corresponding to  
the local ~~in-situ~~ measurements. However, for the Deep Sea and South Namib  
stations, the ~~local~~ measured wind roses exhibit additional components aligned  
with the giant dune orientation visible on the satellite images (Fig. 1c-d).  
Indeed, the analysis of the The time series of wind speed and direction ~~time~~

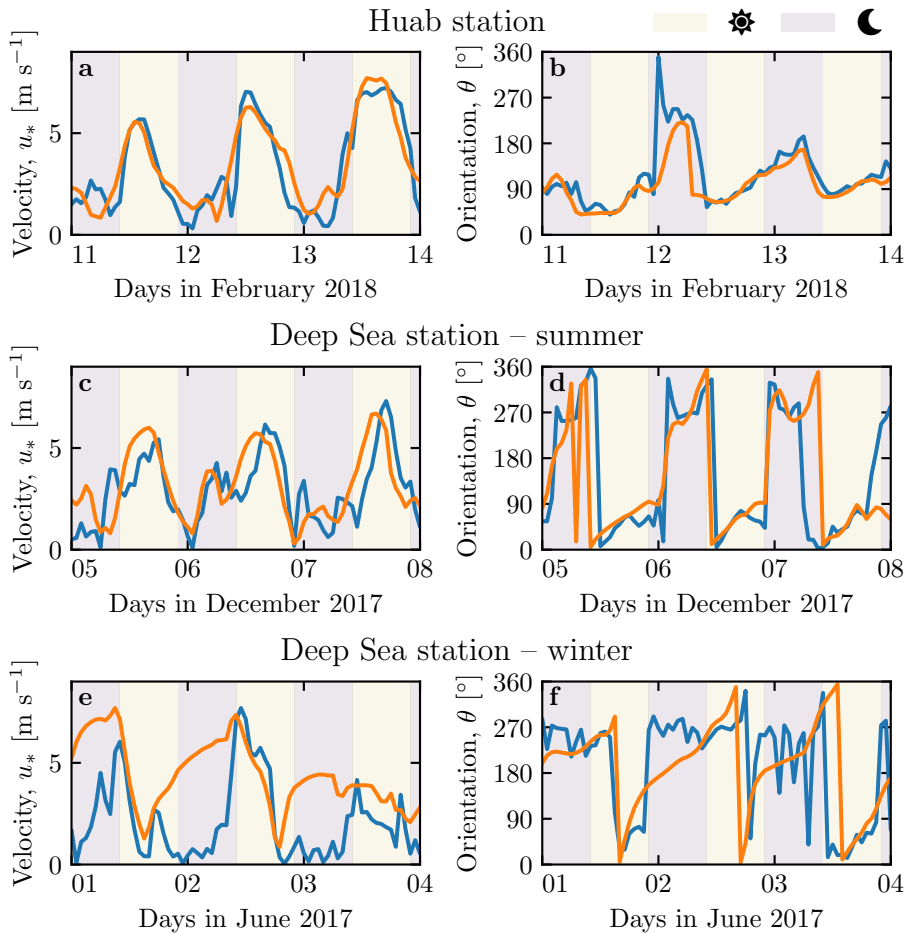


**Fig. 2** Temporal comparison between the wind data coming from the Era5Land climate reanalysis (orange lines) and from the local measurements (blue lines). Color swathes indicate day (between 1000 UTC and 2200 UTC) and night (before 1000 UTC or after 2200 UTC). a–b: Huab station. c–d: Deep Sea station in winter. e–f: Deep Sea station in summer.

168 series shows that the agreement between the local and regional datasets show  
 169 that this agreement in the case of Adamax and Huab stations is always ver-  
 170 ified when no mid-scale topography are present (Fig. 2a–b) and Fig. S5). In  
 171 contrast, for the stations within the giant dune field, we observe that this  
 172 agreement is limited to the Septembre–January time periods (Fig. 2c–d).

### 173 2.3 Influence of the giant dunes on local wind regimes

174 When In the February–August period, when giant dunes are present, in the  
 175 February–August period, the local and regional winds match only during the  
 176 morning during daytime only, i.e when the southerly/southwesterly sea breeze

177 dominates (see Fig. 2(e–f), Fig. 3 and Fig. S6). In the late afternoon and during  
178 the night, when the northwesterly ‘berg’ and katabatic winds blow, ~~the two~~  
179 ~~datasets measurements and predictions~~ differ. In this case, the angular wind  
180 distribution of the local measurements exhibits two additional modes separated  
181 of  $\simeq 180^\circ$ , each corresponding to the giant dune alignment (~~see the~~ purple  
182 frame in Fig. 3 and Fig. S6, as well as Fig. S7). This deviation is also associated  
183 with a global attenuation of the wind strength (Fig. S8). Remarkably, all  
184 these figures show that this process occurs for low wind velocities, typically  
185 for  $u_* < 0.1 \text{ m s}^{-1}$ . For shear velocities larger than  $0.25 \text{ m s}^{-1}$ , this wind  
186 reorientation does not occur. Finally, for intermediate shear velocities, both  
187 reorientation along the dune crest and no reorientation are observed (Fig. S7).

### 188 3 Influence of the circadian cycle of the atmospheric boundary 189 layer

190 ~~In the case of For~~ linear ridges, dune-induced flow disturbances have mainly  
191 been related to the ~~incident wind direction angle between wind direction and~~  
192 ~~crest orientation, with a maximum for angles between  $30^\circ$  and  $70^\circ$~~  (Walker  
193 et al. 2009; Hesp et al. 2015). In our case, ~~it is unlikely to be the dominant~~  
194 ~~parameter, as~~ the most deflected wind for both stations is the most perpen-  
195 ~~icular, where it should be winds with incident directions between  $30^\circ$  and~~  
196  ~~$70^\circ$  (Hesp et al. 2015). An important observation is the difference in behavior~~  
197 ~~such that the incident wind direction does not seem to be the dominant~~  
198 ~~parameter controlling the wind deflection. In contrast, a different behavior~~  
199 ~~is observed between low and high wind velocities, which suggests suggesting~~ a  
200 change in ~~the~~ hydrodynamical regime.

201 Previous studies have linked atmospheric flow around and over topographical  
202 obstacles to the vertical structure of the atmosphere (Stull 1988). More particularly,  
203 ~~dunes evolves in its lower part, the turbulent atmospheric boundary layer~~  
204 ~~(ABL), typically characterized by a logarithmic wind profile and a vertically~~  
205 ~~constant potential temperature. Above, the free atmosphere (FA) is a stably~~  
206 ~~stratified zone in which turbulence is negligible, and where the flow is usually~~  
207 ~~considered as incompressible and inviscid. In the middle, a transitional layer,~~  
208 ~~also known as entrainment zone, is characterized by a sharp increase of the~~  
209 ~~potential temperature, which traps the turbulence resulting from the surface~~  
210 ~~friction below it.~~

211 In the following, we ~~sum-up the dominant numbers discuss the relevant~~  
212 ~~parameters~~ leading to different hydrodynamical interactions with topographi-  
213 cal obstacles, and interpret the data with respect to the corresponding physical  
214 mechanisms.

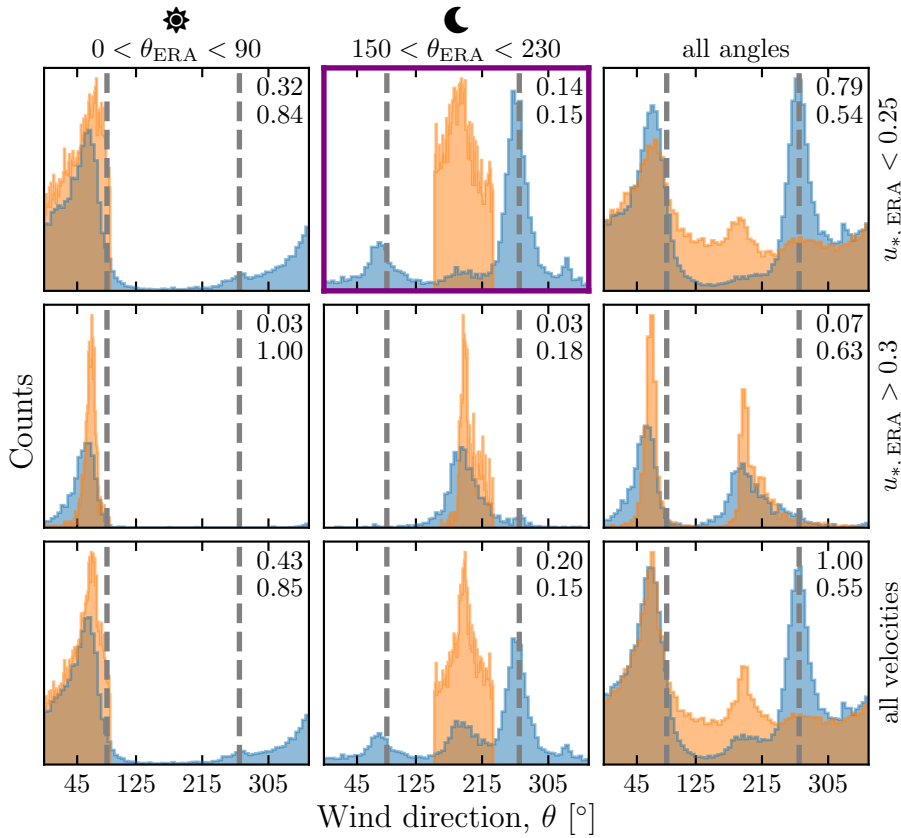


**Fig. 3** Distributions of wind direction at the Deep Sea Station for the Era5Land climate reanalysis (orange) and the local measurements (blue). In each subplot, both distributions are plotted from the same time steps, selected with constraints on the wind direction (columns) and/or wind velocity (rows) of the Era5Land dataset. The gray vertical dashed lines indicate the dune orientation, ~~and~~. The numbers at the top right numbers give the percentage of the total number of time steps selected in each subplot sub-range, as well as the percentage of them corresponding to the day (between 1000 UTC and 2200 UTC). The purple frame highlights the regime (small wind velocities, nocturnal summer wind) in which the data from both datasets differs. A similar figure can be obtained for the Deep Sea station (see Fig. S6).

215 3.1 Relevant non-dimensional parameters and physical  
216 modeling considerations

217 Flow deflection over ridges can be simplistically understood from a balance  
218 between inertia and pressure gradientsunderstood from the Bernoulli principle (Hesp  
219 et al. 2015). As the flow approaches the ridge crest, the compression of the  
220 streamlines results in larger flow velocities, and thus lower pressures (Rubin  
221 and Hunter 1987). An incident flow oblique to the ridge is then deflected to  
222 towards lower pressure zones, i.e towards the crest. Turbulent dissipation at the  
223 bottom and non-linearities tends to increase this effect downstream, resulting

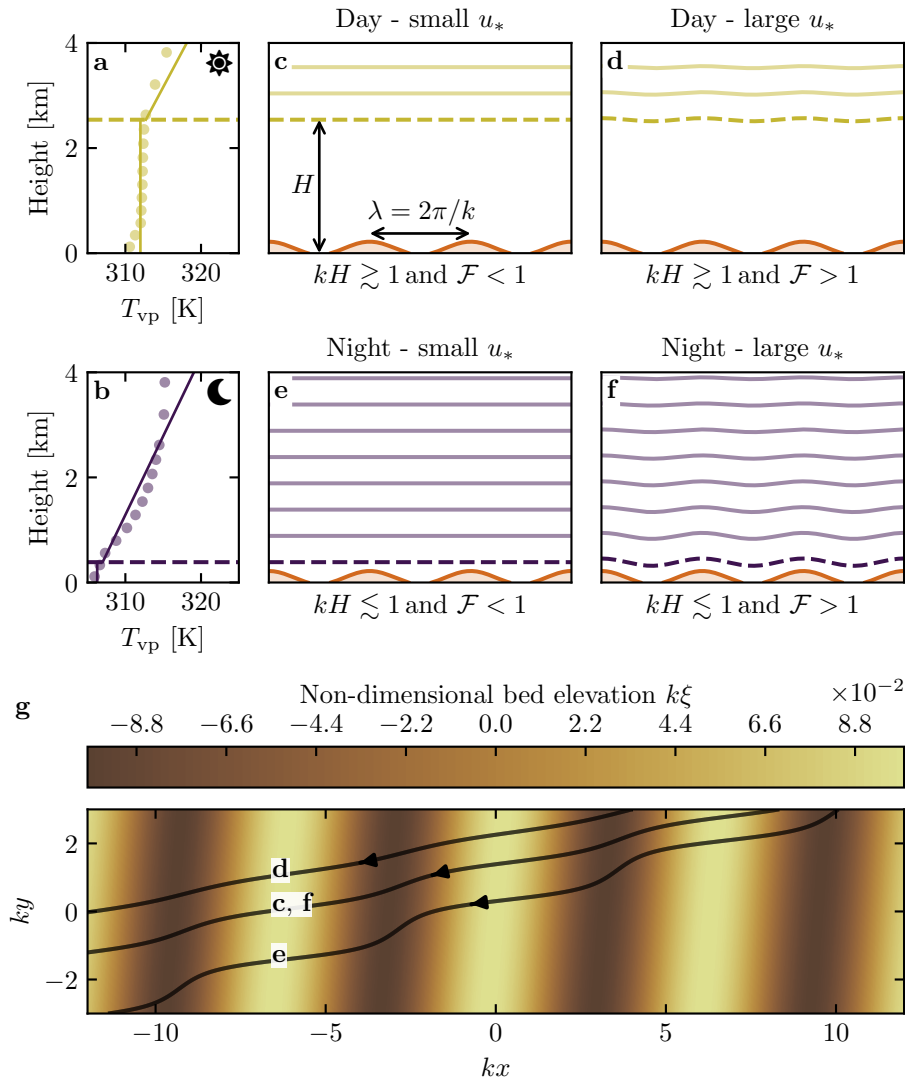


**Fig. 4** a–b: Vertical profiles of the virtual potential temperature at 2 different time steps (blue day - 29/03/2017 - 1100–1200 UTC, red night - 21/03/2017 - 1200–2200 UTC) at the Deep Sea station. Dots: data from the ERA5 reanalysis. Transparent dashed lines: boundary layer height given by the ERA5 reanalysis, calculated from the bulk Richardson number (Seidel et al. 2012). Plain lines: vertical (boundary layer) and linear (free atmosphere) fits to estimate the stratification properties. c–f: Sketches representing the interaction between the giant dunes and the atmospheric flow for different meteorological conditions. g: Streamlines qualitatively representing the effect of low, medium and high flow confinement, in the case of the Deep Sea station. The red lines are calculated from the unconfined case similar to d. The sinuous blue line represents a confined case similar to f. For details on the streamline derivation, see Appendix 5.

in along the crest wind deflection in the lee side (Hesp et al. 2015; Gadal et al. 2019).

Another way to increase the flow deflection is its confinement below a capping surface, that results in further streamline compression. This happens when is the case for bedforms forming in open channel flows such as rivers (Fourrière et al. 2010; Unsworth et al. 2018), but also for eolian dunes. These dunes evolve in the turbulent atmospheric boundary layer (ABL), which is capped by a transitional layer separating it from the stratified atmosphere above (see Fig. 4). Two different mechanisms control the possibility of this additional streamline compression.

On one hand, it depends if the flow disturbance induced by the obstacle reaches underlying topography reach the surface. As obstacles typically disturb flow over a characteristic height similar to their widthlength, the potential of interaction between the dunes and the overlying atmospheric structure surface is well captured by the parameter  $kH$ , where  $k = 2\pi/\lambda$  is the wavenumber and  $H$  the ABL depth. Note that  $H$  is directly related to the radiative fluxes at the Earth surface, and thus varies with the circadian and seasonal cycles. Here, the giant dunes have kilometric wavelengths, such that  $0.02 \lesssim kH \lesssim 5$ , and they interact most of the time with the capping layer and the stratified free atmosphere (FA) above (Andreotti et al. 2009).

Note that the ability of Interestingly, the limit of no-interactions between the topography and the capping layer and stratification to accommodate a perturbation induced by the topography directly impacts the strength of this confinement effect (Fig. 4) boundary layer structure ( $kH \gg 1$ ), in which the properties of the overlying atmospheric structure are irrelevant, is never reached here, in the case of giant dunes.

On the other hand, it depends on rigidity of the capping surface, as its deformation releases the confinement effect inducing streamline compression. This is typically quantified using surface and internal Froude numbers—the Froude number (Vosper 2004; Stull 2006; Sheridan and Vosper 2006; Hunt et al. 2006; Jiang 2014):

$$\mathcal{F}_{rs} = \frac{U}{\sqrt{\frac{\Delta\rho}{\rho} g H}}, \quad \mathcal{F}_{ri} = \frac{kU}{N} \frac{U}{\sqrt{\frac{\Delta\rho}{\rho_0} g H}}, \quad (1)$$

where  $U$  is the wind velocity at the top of the ABL,  $\rho-\rho_0$  its average density,  $\Delta\rho$  the density jump between the ABL and the FA and  $N$  is the Brunt-Väisälä frequency, characteristic of the stratification.

The smallest wind disturbances are expected during the day, when the ABL depth is comparable to the dune wavelength ( $kH \gtrsim 1$ ) and for large wind velocities, which correspond to a weak confinement situation (Fig. 4d). On the contrary, large wind disturbances are expected to occur during the night, when the confinement is mainly induced by shallow ABL (Fig. 4e–f). Note that this strong confinement can be somewhat reduced in the case of strong winds (corresponding to large Froude numbers, see Fig. 4f), explaining the

264 threshold in velocity transition from deflected to non-deflected winds related  
 265 to low and high velocities observed in the data (see section 2.3).

266 3.2 Flow regime diagrams

267 To highlight these different regimes from our data, we compute wind disturbance  
 268 diagrams in the space defined by the three two relevant non-dimensional  
 269 numbers presented above,  $(kH, Fr_S, Fr_I)$  ( $kH, \mathcal{F}$ ). Those are calculated from  
 270 the time series of the geopotential, temperature and specific humidity vertical  
 271 profiles available in the ERA5 climate reanalysis (see SI section 2). Flow de-  
 272 viation is computed as the minimal angle between the wind orientations from  
 273 the two datasets:

$$\delta_\theta = |\min ([\theta_{\text{ERA}} - \theta_{\text{station}}] \bmod 360, [\theta_{\text{station}} - \theta_{\text{ERA}}] \bmod 360)|.$$

274 local measurements, and the regional predictions. The relative velocity mod-  
 275 ulation is computed as

$$\delta_u = \frac{u_*^{\text{ERA}} - u_*^{\text{station}}}{u_*^{\text{ERA}}}. \quad (2)$$

276 As both Froude numbers have qualitatively the same impact on the flow  
 277 confinement, we first leave aside the internal Froude number, and focus on the  
 278 space  $(kH, Fr_S)$ . When representing the two variables  $\delta_\theta$  and  $\delta_u$  in this space,  
 279 different regime emerges (Fig. 5). Small wind disturbances ( $\delta_\theta \rightarrow 0, \delta_u \rightarrow 0$ ) are  
 280 located in the top-right part of the diagrams, corresponding to a regime mixing  
 281 low-interaction and low-confinement ( $kH$  and  $Fr_S$  large enough, Fig. 4d).  
 282 Lower values of  $kH$  (stronger interaction) or Froude numbers number (stronger  
 283 confinement) then both leads lead to an increase in wind disturbances, both in  
 284 terms of orientation and velocity. Below a threshold value of  $kH \simeq 0.3$ , wind  
 285 disturbance occurs independently of the Froude numbers value. Furthermore,  
 286 this also seems to control a transition between number value, probably due to  
 287 enhanced non-linear effects linked to strong flow modulation by the obstacle  
 288 in this part of the diagram. The Froude number also controls a transition from  
 289 damped to amplified wind velocities within the interdune in the interdune, with  
 290 a transition at  $\mathcal{F} \simeq 0.4$  (Fig. 5b), for which we do not have an explanation.  
 291 Note that the same interpretation can be done with the diagrams including  
 292 the internal Froude number  $Fr_I$ , as shown by Fig. S12.

293 Interestingly, the limit of no interactions between the topography and the  
 294 boundary layer structure ( $kH \gg 1$ ), in which the properties of the capping  
 295 layer and the stratification become irrelevant, is never reached here, in the  
 296 ease of giant dunes. This may be linked to a transition in the flow regime in  
 297 the lee side of the obstacle (lee waves, hydraulic jumps, rotors) but further  
 298 measurements are needed in order to assess this (Baines 1995; Vosper 2004).

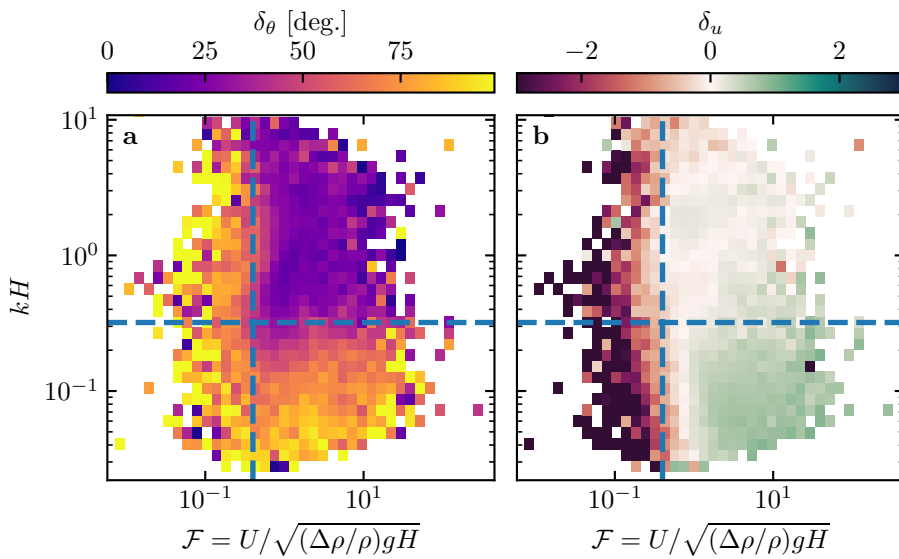


**Fig. 5** Regime diagrams of the wind deviation  $\delta_\theta$  and relative attenuation/amplification  $\delta_u$  in the space  $(\mathcal{F}, kH)$ , containing the data from both the Deep Sea and South Namib stations. Blue dashed lines empirically delimit the different regimes. The point density in each bin of the diagrams is shown in Fig. S11. The regime diagrams in the spaces  $(\mathcal{F}_1, kH)$  and  $(\mathcal{F}_1, \mathcal{F})$  are shown in Fig. S12.

### 299 3.3 On the influence of the stratification of the free atmosphere

300 The presence of a stratification in the free atmosphere can also impact the  
 301 flow confinement, depending on its ability to deform under the presence of an  
 302 underlying obstacle. This can be quantified using the internal Froude number (Vosper 2004; Stull 2006; Sheridan and Vosp  
 303 ;

$$\mathcal{F}_I = \frac{kU}{N}, \quad (3)$$

304 where  $N = \sqrt{-(g/\rho_0)(\partial\rho/\partial z)}$  is characteristic of the stratification. Both Froude  
 305 numbers have the same qualitative effect on flow confinement, as they quantify  
 306 the rigidity of the overlying layers. This is confirmed by figure S12, where  
 307 we can also find the different regimes related to wind disturbances described  
 308 previously for the Froude number  $\mathcal{F}$ .

## 309 4 Discussion

## 310 5 Discussion

311 The comparison of local (direct measurements) and regional (climate reanalysis)  
 312 wind data reveals the giant dunes feedback on the flow. In flat areas, the  
 313 matching between ~~both datasets – measurements and prediction~~ confirms the

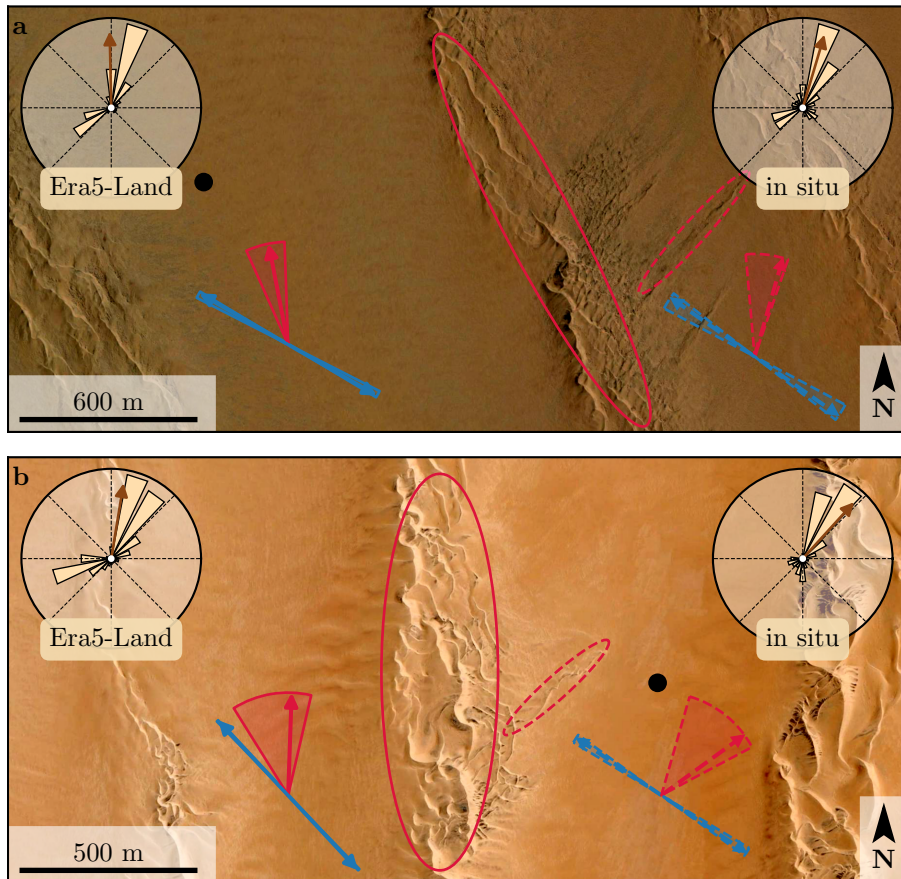


**Fig. 6** Regime diagrams of implications for smaller scale patterns in (a) the **South Namib** and (b) **Deep Sea**. The ellipses indicates the space ( $F_{rs}, kH$ ) different types of elongating dunes, containing at large (plain) and small scale (dashed). The dune orientations are calculated using the **data** model of Courrech du Pont et al. (2014) from both the **Deep Sea** sand flux angular distributions, shown here for typical sand quartz grains of  $180 \mu\text{m}$ . The double blue and **South Namib stations** single red arrows correspond to the two possible dune growth mechanisms, bed instability and elongation, respectively. Likewise, plain arrows are calculated from the ERA5-Land data, and dashed lines empirically delimit arrows from the different regimes local measurements. The point density in each bin of Wedges show the diagrams is shown uncertainty on the orientation calculation, and the arrows correspond to typical parameters found in Fig the literature, i.e. a grain diameter of  $180 \mu\text{m}$  and a flux-up ratio of 1.6. The regime diagrams in black dots indicate the spaces ( $F_{ri}, kH$ ) and ( $F_{ri}, F_{rs}$ ) are shown in Fig position of the measurement stations. See Appendix 2 for additional details.

ability of the ERA5Land climate reanalysis to predict the wind flow down to scales  $\sim 10$  km, i.e the grid model. When smaller scale topographies are present (giant dunes in our case), locally measured wind regimes ~~may can~~ significantly differ from the ~~regional~~regionally predicted ones. Furthermore, we link these disturbances induced by the dunes to their interaction with the lower part of the atmospheric vertical structure, and more specifically to its circadian variability. During the night, the presence of a shallow atmospheric boundary layer (ABL) induces a strong ~~flow-confinement~~confinement of the flow, associated with large wind deviation and acceleration or deceleration. During the day, the capping layer is high enough to prevent its interaction with the giant dunes, resulting in a low ~~flow-confinement~~confinement of the flow, and thus smaller wind disturbances. Interestingly, we also found that this effect could be counterbalanced by the presence of large wind velocities, capable of deforming the capping layer and/or the FA stratification, thus decreasing the confinement effect.

Simple linear models ~~such as the one of Andreotti et al. (2009) also suggests also suggest~~ that larger wind disturbances occur under strong flow confinement such as described above Andreotti et al. (2009, 2012). However, they are unable to reproduce the magnitude of the observed deviations, probably due to the presence of hydrodynamical non-linear effects, ~~negligible in low confinement situations, but not otherwise all the more present in high confinement situations linked to strong flow modulations~~ (see Fig. S12 and Appendix 1). ~~Additionally, note that the They also predict different spatial flow structures associated with the dune feedback on the wind can not be studied with our single point such as lee waves and rotors (Baines 1995; Vosper 2004)~~, which are likely to be complicated by these non-linearities, and which ~~cannot be observed by our single point~~ measurements. Measurements in different places ~~on and near the same topographical obstacle along and across the ridge~~ are then needed ~~for in order to properly map these flow structures, and allow~~ further comparisons with models.

This study highlights the interaction between giant dunes and the atmospheric boundary layer, ~~supporting as well the way~~. It then supports the debated idea that the capping layer acts as a bounding surface limiting dune growth (Andreotti et al. 2009; Gunn et al. 2021)~~– (Andreotti et al. 2009)~~, as opposed to an unconstrained growth ever-slower with size (Eastwood et al. 2011; Gunn et al. 2021). Once validated, this mechanism would then allow inference of the ABL depth from the giant bedforms spacing where measurements are not feasible or available, as performed by Lorenz et al. (2010) on Titan.

This interaction also have implications at smaller scales, where bedformsthen develop from the wind disturbed by the giant dunes, instead of the regional wind regime. Differences strong implications for smaller scales bedforms, as illustrated in Fig. 6. In the Namib Sand Sea, small linear dunes ( $\sim 50$  m-wide) are present in the interdune between giant linear dunes ( $\sim 2$  km-wide). While differences between larger and smaller scale dune patterns are observed ubiquitously. As larger dunes are often older than smaller ones, sometimes this discrepancy have been previously attributed to climatic changes in wind

360 regimes (?), they are now largely attributed to the presence of two different  
361 dune growth mechanisms, leading to two different dune patterns (orientations  
362 and/or morphologies) for the same wind regime (Courrech du Pont et al. 2014; Runyon et al. 2017; Lü et al. 2017; Song e  
363 . Here, using this feedback mechanism, we suggest that current winds are also  
364 able to explain dune patterns at all scales. For example, this seems to be  
365 the case for the linear dunes ( $\sim 50$  m wide) elongating within the interdune  
366 between two coupling sediment transport and dune growth models, we show  
367 that the orientations of the small and giant linear dunes ( $\sim 2$  km wide) in the  
368 Namib Sand Sea (see can be predicted from the same dune growth mechanism,  
369 using the locally measured and regionally predicted winds, respectively (red  
370 arrows in Fig. 6).

371 Implications for smaller scale patterns in (a) the South Namib and (b)  
372 Deep Sea. The ellipses indicates the different types of elongating dunes, at  
373 large (plain) and small scale (dashed). The dune orientations are calculated  
374 using the model of Courrech du Pont et al. (2014) from the sand flux angular  
375 distributions, shown here for typical sand quartz grains of  $180 \mu\text{m}$ . The double  
376 blue and single red arrows correspond to the two possible dune growth mechanisms,  
377 bed instability and elongation, respectively. Likewise, plain arrows are calculated  
378 from the ERA5-Land datasets, and dashed arrows from the in situ measurements.  
379 Wedges show the uncertainty on the orientation calculation, and the arrows  
380 correspond to typical parameters found in the literature, i.e a grain diameter  
381 of  $180 \mu\text{m}$  and a flux-up ratio of 1.6. The green dots indicate the position of the  
382 measurement stations. See Appendix 2 for additional details. The giant dune  
383 feedback on the flow described in this study then provides a mechanism for the  
384 existence of these small linear dunes elongating across the interdune, as yet  
385 unresolved. While further studies are needed, these dune type could provide  
386 additional strong constraints for the inference of local winds from bedforms, as  
387 currently performed on Mars using ripple orientations (Liu and Zimbelman 2015; Hood et al. 2021)  
388 ~

389 **Acknowledgements** These should follow the concluding section of the paper and precede  
390 the References and any appendices, if they are present. The acknowledgements section does  
391 not require a section number. We would like to acknowledge the contributors of the following  
392 open-source python libraries. Matplotlib (Hunter 2007), Numpy (Harris et al. 2020) and  
393 Scipy (Virtanen et al. 2020), which provide an incredibly efficient ecosystem allowing scientific  
394 research in Python.

395 Era5 and Era5Land datasets are publicly available at the Copernicus Climate Change  
396 Service (C3S) Climate Data Store. The locally measured wind data can be found at upload on public data repository.  
397 The digital elevation models from the Shuttle Radar Topography Mission are publicly  
398 available from Nasa servers, and can be downloaded at <https://dwtkns.com/srtm30m/>. Fully  
399 documented codes used to analyze this study are available at <https://github.com/Cgadal/GiantDunes>  
400 (will be made public upon acceptance of this manuscript for publication).

401 [citing all grants ...]  
402

403 **Appendix 1: ABL turbulent wind model**

404 Following the work of Fourrière et al. (2010) and Andreotti et al. (2012), Andreotti et al. (2012)  
 405 and Andreotti et al. (2009), we briefly expose in this section the linear response  
 406 of a turbulent flow to a small aspect ratio perturbation of the topography  
 407 underlying topography. As this topography can be decomposed into several  
 408 sinusoidal modes, we focus on the response to a sinusoidal topography as:

$$\xi = \xi_0 \cos [k (\cos(\alpha)x + \sin(\alpha)y)], \quad (4)$$

409 which is also a good approximation to-for the giant dunes observed in the  
 410 Deep Sea and South Namib Station (see Fig 1 and Fig S4). Here,  $x$  and  $y$  are  
 411 the streamwise and spanwise coordinates,  $k = 2\pi/\lambda$  the wavenumber of the  
 412 sinusoidal perturbation, and  $\alpha$  its crest orientation, calculated with respect to  
 413 the  $y$ -direction.

414 In terms of The two components of the basal shear stress  $\tau = \rho u_*^2$ , the  
 415 flow response can then generally be written in  $\tau = \rho_0 u_* u_*$ , constant in a flat  
 416 bottom situation, can then be written without loss of generality as:

$$\tau_x = \tau_0 \left( 1 + k \xi_0 \sqrt{\mathcal{A}_x^2 + \mathcal{B}_x^2} \cos [k (\cos(\alpha)x + \sin(\alpha)y) + \phi_x] \right), \quad (5)$$

$$\tau_y = \tau_0 k \xi_0 \sqrt{\mathcal{A}_y^2 + \mathcal{B}_y^2} \cos [k (\cos(\alpha)x + \sin(\alpha)y) + \phi_y], \quad (6)$$

417 where  $\tau_0$  is the basal shear stress on a flat bed, and  $\phi_{x,y} = \tan^{-1} (\mathcal{B}_{x,y}/\mathcal{A}_{x,y})$ .  
 418 The in-phase and in-quadrature hydrodynamical coefficients  $\mathcal{A}_{x,y}$  and  $\mathcal{B}_{x,y}$   
 419 are functions of the flow conditions, i.e the bottom roughness, the free surface  
 420 vertical flow structure or the incident flow direction (Fourrière et al. 2010; Andreotti et al. 2009, 2012; ?)  
 421 (Fourrière et al. 2010; Andreotti et al. 2009, 2012).

422 Andreotti et al. (2012) have shown that Following Andreotti et al. (2012)  
 423 the impact of the incident wind direction can be well approximated by the  
 424 following expressions:

$$\mathcal{A}_x = \mathcal{A}_0 \cos^2 \alpha, \quad (7)$$

$$\mathcal{B}_x = \mathcal{B}_0 \cos^2 \alpha, \quad (8)$$

$$\mathcal{A}_y = \frac{1}{2} \mathcal{A}_0 \cos \alpha \sin \alpha, \quad (9)$$

$$\mathcal{B}_y = \frac{1}{2} \mathcal{B}_0 \cos \alpha \sin \alpha, \quad (10)$$

425 where  $\mathcal{A}_0$  and  $\mathcal{B}_0$  are now two coefficients independent of the dune orientation  $\alpha$ . In the case of a fully turbulent boundary layer capped by a free  
 426 atmosphere capping stratified atmosphere, they now only depend on  $kH$ ,  $kz_0$ ,  
 427  $\mathcal{F}_{r1}$  and  $\mathcal{F}_{rS}$ , as detailed by Andreotti et al. (2009). More specifically, their  
 428 variation in the marginal spaces ( $kH, \mathcal{F}_{rS}$ ) and ( $kH, \mathcal{F}_{r1}$ ) are shown  $\mathcal{F}$  and  
 429  $\mathcal{F}_L$  Andreotti et al. (2009). In this study, we assume a constant hydrodynamic  
 430 roughness  $z_0 \sim 1$  mm, leading to a constant value of  $kz_0 \sim 10^{-6}$ . Measured  
 431 values of  $z_0$  in the field indeed reports a variation of  $z_0$  between 0.1 mm and

10 mm (Sherman and Farrell 2008; Field and Pelletier 2018), but  $\mathcal{A}_0$  and  $\mathcal{B}_0$  does not vary much in the corresponding range of  $kz_0$  (Fourrière et al. 2010). Note that the linearity assumption of this theoretical framework requires  $(|\tau| - \tau_0)/\tau_0 \ll 1$ , which is satisfied by  $k\xi\sqrt{\mathcal{A}_0^2 + \mathcal{B}_0^2} \ll 1$ . In our case, the giant dune morphology gives  $k\xi \simeq 0.1$ , setting the upper bound of the coefficient modulus  $\sqrt{\mathcal{A}_0^2 + \mathcal{B}_0^2}$  to 10.

Additionally, we also calculate the time series of the hydrodynamical coefficients from the time series of the non-dimensional numbers used in this study. The results, shown Fig. S12 under the similar form of the regime diagrams presented in Fig. S12.

Typical values for the unconfined case are therefore  $\mathcal{A}_0 = 3.4$  and  $\mathcal{B}_0 = 1$ . In our case of giant dunes with  $k\xi_0 \sim 0.1$ , significant wind disturbances are then expected when  $\sqrt{\mathcal{A}_0^2 + \mathcal{B}_0^2} \sim 105$  and Fig. S12, exhibit a qualitative matching with the observations presented in this study. Small values of these coefficients ( $\mathcal{A}_0 \simeq 3.4$  and  $\mathcal{B}_0 \simeq 1$ ) are found in low confinement cases, i.e for  $kH \gg 1$  (no interaction between the dunes and the capping layer) or for  $kH \gg 1$  but large enough Froude numbers (reduced flow confinement due to the deformation of the overlying capping layer and stratification). In contrast, larger values are obtained in high confinement cases (small  $kH$  and Froude numbers). However, this is also the limit not that most of this part of the diagrams are outside of the linear regime where this theoretical model is applicable, as hydrodynamical non-linearities become significant when  $k\xi_0\sqrt{\mathcal{A}_0^2 + \mathcal{B}_0^2} \sim 1$  limit discussed above ( $\sqrt{\mathcal{A}_0^2 + \mathcal{B}_0^2} \gtrsim 10$ ), which does not allow further quantitative comparison with the data.

## Appendix 2: Sediment transport and dune morphodynamics

Here, we briefly detail describe the sediment transport and dune morphodynamics theoretical framework leading to the prediction of sand fluxes and dune orientations from wind data.

The sediment fluxes can been directly linked to the wind basal shear stress at each time steps  $t$  from transport laws, whose exact forms depends on the sediment transport mechanisms taken into account. In this work, we following the recent work of Pähzt and Durán (2020), where the sediment flux  $q_{\text{sat}}$  on a flat bed made of loose sand can be expressed as:

*Sediment transport* The prediction of sand fluxes from wind data has been a long standing issue in geomorphological studies (Fryberger and Dean 1979; Pearce and Walker 2005; Sherman and Li 2011). Based on laboratory studies in wind tunnels (Rasmussen et al. 1996; Iversen and Rasmussen 1999; Creysse et al. 2009), as well as physical considerations (Ungar and Haff 1987; Andreotti 2004; Durán et al. 2011; Pähzt and Durán 2020) it has been shown that the steady saturated sand flux over a flat sand bed depends linearly on the shear stress:

$$\frac{q_{\text{sat}, t}}{Q} = \frac{2\sqrt{\Theta_{\text{th}}}}{\kappa\mu} \Omega\sqrt{\Theta_{\text{th}}} (\Theta_t - \Theta_{\text{th}}) \frac{1 + \frac{C_M}{\mu}\Theta_t - \Theta_{\text{th}}}{\mu}, \quad (11)$$

where  $\kappa = 0.4$  is the von Kármán constant,  $C_M = 1.7$  a constant,  $Q = d\sqrt{(\rho_s - \rho)gd/\rho}$  is a proportionality constant,  $Q = d\sqrt{(\rho_s - \rho_0)gd/\rho_0}$  is a characteristic flux, with  $\Theta = \rho_0 u_{*,t}^2 / (\rho_s - \rho_0)gd$  the Shields number, and  $\Theta_{th}$  its threshold value for incipient sediment transport. Here,  $\rho_s = 2.6 \text{ g cm}^{-3}$  and  $d = 180 \mu\text{m}$  are the grain density and diameter, and  $g$  is the gravitational acceleration. The friction coefficient

Recently, Pähzt and Durán (2020) suggested a quadratic dependency on the shear stress by taking into account grain-grain interactions within the transport layer, performing better at reproducing laboratory data at high wind velocities:

$$\frac{q_{sat,t}}{Q} = \frac{2\sqrt{\Theta_{th}}}{\kappa\mu} (\Theta_t - \Theta_{th}) \left( 1 + \frac{C_M}{\mu} [\Theta_t - \Theta_{th}] \right), \quad (12)$$

where  $\kappa = 0.4$  is the von Kármán constant,  $C_M = 1.7$  a constant and  $\mu$  is a friction coefficient, taken to be the avalanche slope of the granular material, i.e.  $\sim 0.6$ . Finally, the Shields number is defined as  $\Theta = \rho u_{*,t}^2 / (\rho_s - \rho)gd$ , and its threshold value for incipient sediment transport as been calibrated using laboratory experiments to The fit of this law to the experimental data of Creyssels et al. (2009) and Ho et al. (2011) gives  $\Theta_{th} = 0.0035$ . The sand flux angular distributions and the dune orientations in Fig. 6 are calculated using this quartic law (12). However, we verified that using the quadratic law (11) instead did not change the predicted dune orientations by more than a few degrees.

*Dune orientations* The dune orientations are then predicted from the computed sand flux time series, using the dimensional model of Courrech du Pont et al. (2014). Two orientations are possible depending on the mechanism dominating the dune growth: elongation or bed instability (the latter is also known as the rule of maximum gross bedform-normal transport from Rubin and Hunter (1987)).

The orientation  $\alpha$  corresponding the bed instability is then the one that maximizes the following growth rate:

$$\sigma \propto \frac{1}{HWT} \frac{1}{H_d W_d T} \int_t q_{crest,t} |\sin(\theta_t - \alpha)|, \quad (13)$$

where  $H$  and  $W$   $H_d$  and  $W_d$  are dimensional constants representing the dune height and width, respectively. The flux at the crest is expressed as:

$$q_{crest,t} = q_{sat,t} [1 + \gamma |\sin(\theta_t - \alpha)|], \quad (14)$$

where the flux-up ratio  $\gamma$  has been calibrated to 1.6 using field studies, underwater laboratory experiments and numerical simulations. Similarly, the dune orientation corresponding to the elongation mechanism is the one that verifies:

$$\tan(\alpha) = \frac{\langle q_{crest,t}(\alpha) e_{\theta_t} \rangle \cdot e_{WE}}{\langle q_{crest,t}(\alpha) e_{\theta_t} \rangle \cdot e_{SN}}, \quad (15)$$

505 where  $\langle \cdot \rangle$  denotes a vectorial time average. The unitary vectors  $e_{WE}$ ,  $e_{SN}$  and  
506  $e_{\theta_t}$  are in the West–East, South–North and wind direction, respectively.

507 The resulting computed dune orientations, blue and red arrows in figure 6,  
508 are however then depending on a large certain number of parameters (grain  
509 properties, flux-up ratio), for which we took typical values for eolian desert  
510 on Earth. Due to the lack of measurements in the studied places, significant  
511 uncertainties can however be expected. We therefore run a sensibility test by  
512 calculating the dune orientations for grain diameters ranging from 100  $\mu\text{m}$   
513 to 400  $\mu\text{m}$  and the speed-up ratio from 0.1 to 10 (wedges on figure 6). We  
514 also checked the sensibility the transport law by repeating the process with  
515 the quadratic transport also used for comparison in Pähzt and Durán (2020),  
516 which led to no more than n% of variation with respect to .

**517 References**

- 518 Andreotti B (2004) A two-species model of aeolian sand transport. *J Fluid  
519 Mech* 510(510):47–70, DOI 10.1017/S0022112004009073
- 520 Andreotti B, Fourrière A, Ould-Kaddour F, Murray B, Claudin P (2009) Gi-  
521 ant aeolian dune size determined by the average depth of the atmospheric  
522 boundary layer. *Nature* 457(7233):1120–1123
- 523 Andreotti B, Claudin P, Devauchelle O, Durán O, Fourrière A (2012) Bedforms  
524 in a turbulent stream: ripples, chevrons and antidunes. *Journal of Fluid  
525 Mechanics* 690:94–128
- 526 Ashkenazy Y, Yizhaq H, Tsoar H (2012) Sand dune mobility under climate  
527 change in the kalahari and australian deserts. *Climatic Change* 112(3):901–  
528 923
- 529 Bacik KA, Lovett S, Colm-cille PC, Vriend NM (2020) Wake induced long  
530 range repulsion of aqueous dunes. *Physical review letters* 124(5):054,501
- 531 Baines PG (1995) Topographic effects in stratified flows. Cambridge university  
532 press
- 533 Blumberg DG, Greeley R (1996) A comparison of general circulation model  
534 predictions to sand drift and dune orientations. *Journal of Climate*  
535 9(12):3248–3259
- 536 Claudin P, Wiggs GFS, Andreotti B (2013) Field evidence for the upwind  
537 velocity shift at the crest of low dunes. *Boundary-layer Meteorol* 148(1):195–  
538 206, DOI 10.1007/s10546-013-9804-3
- 539 Courrech du Pont S (2015) Dune morphodynamics. *Comptes Rendus Physique*  
540 16(1):118–138
- 541 Courrech du Pont S, Narteau C, Gao X (2014) Two modes for dune orientation.  
542 *Geology* 42(9):743–746
- 543 Creyssels M, Dupont P, El Mohtar AO, Valance A, Cantat I, Jenkins JT, Pasini  
544 JM, Rasmussen KR (2009) Saltating particles in a turbulent boundary layer:  
545 experiment and theory. *Journal of Fluid Mechanics* 625:47–74
- 546 Dee DP, Uppala SM, Simmons AJ, Berrisford P, Poli P, Kobayashi S, Andrae  
547 U, Balmaseda M, Balsamo G, Bauer dP, et al. (2011) The era-interim re-  
548 analysis: Configuration and performance of the data assimilation system.  
549 *Quarterly Journal of the royal meteorological society* 137(656):553–597
- 550 Durán O, Claudin P, Andreotti B (2011) On aeolian transport: Grain-scale  
551 interactions, dynamical mechanisms and scaling laws. *Aeolian Research*  
552 3(3):243–270, DOI 10.1016/j.aeolia.2011.07.006
- 553 Durran DR (1990) Mountain waves and downslope winds. In: *Atmospheric  
554 processes over complex terrain*, Springer, pp 59–81
- 555 Eastwood E, Nield J, Baas A, Kocurek G (2011) Modelling controls on aeolian  
556 dune-field pattern evolution. *Sedimentology* 58(6):1391–1406
- 557 Farr TG, Rosen PA, Caro E, Crippen R, Duren R, Hensley S, Kobrick M,  
558 Paller M, Rodriguez E, Roth L, et al. (2007) The shuttle radar topography  
559 mission. *Reviews of geophysics* 45(2)
- 560 Fernando H, Mann J, Palma J, Lundquist JK, Barthelmie RJ, Belo-Pereira M,  
561 Brown W, Chow F, Gerz T, Hocut C, et al. (2019) The perdigao: Peering

- 562 into microscale details of mountain winds. *Bulletin of the American Meteorological Society* 100(5):799–819  
563
- 564 Field JP, Pelletier JD (2018) Controls on the aerodynamic roughness length  
565 and the grain-size dependence of aeolian sediment transport. *Earth Surface  
566 Processes and Landforms* 43(12):2616–2626, DOI 10.1002/esp.4420  
567
- 568 Fourrière A, Claudin P, Andreotti B (2010) Bedforms in a turbulent stream:  
569 formation of ripples by primary linear instability and of dunes by nonlinear  
570 pattern coarsening. *Journal of Fluid Mechanics* 649:287–328  
571
- 572 Frederick KA, Hanratty TJ (1988) Velocity measurements for a turbulent non-  
573 separated flow over solid waves. *Experiments in fluids* 6(7):477–486  
574
- 575 Fryberger SG, Dean G (1979) Dune forms and wind regime. A study of global  
576 sand seas 1052:137–169  
577
- 578 Gadal C, Narteau C, Courrech Du Pont S, Rozier O, Claudin P (2019) Incip-  
579 ient bedforms in a bidirectional wind regime. *Journal of Fluid Mechanics*  
580 862:490–516  
581
- 582 Gunn A, Wanker M, Lancaster N, Edmonds DA, Ewing RC, Jerolmack DJ  
583 (2021) Circadian rhythm of dune-field activity. *Geophysical Research Letters*  
584 48(5):e2020GL090,924  
585
- 586 Harris CR, Millman KJ, van der Walt SJ, Gommers R, Virtanen P, Cournapeau D,  
587 Wieser E, Taylor J, Berg S, Smith NJ, et al. (2020) Array program-  
588 ming with numpy. *Nature* 585(7825):357–362  
589
- 590 Hersbach H, Bell B, Berrisford P, Hirahara S, Horányi A, Muñoz-Sabater  
591 J, Nicolas J, Peubey C, Radu R, Schepers D, et al. (2020) The era5  
592 global reanalysis. *Quarterly Journal of the Royal Meteorological Society*  
593 146(730):1999–2049  
594
- 595 Hesp PA, Smyth TAG, Nielsen P, Walker IJ, Bauer BO, Davidson-Arnott R  
596 (2015) Flow deflection over a foredune. *Geomorphology* 230:64–74  
597
- 598 Ho TD, Valance A, Dupont P, Ould El Moctar A, Tuan Duc H, Valance A,  
599 Dupont P, Ould El Moctar A (2011) Scaling laws in aeolian sand transport.  
600 *Physical Review Letters* 106(9):4–7, DOI 10.1103/PhysRevLett.106.094501  
601
- 602 Hood DR, Ewing RC, Roback KP, Runyon K, Avouac JP, McEnroe M (2021)  
603 Inferring airflow across martian dunes from ripple patterns and dynamics.  
604 *Frontiers in Earth Science* 9:Art-No  
605
- 606 Howard AD (1977) Effect of slope on the threshold of motion and its applica-  
607 tion to orientation of wind ripples. *Geological Society of America Bulletin*  
608 88(6):853–856  
609
- 610 Hu Z, Gao X, Lei J, Zhou N (2021) Geomorphology of aeolian dunes in the  
611 western sahara desert. *Geomorphology* 392:107,916  
612
- 613 Hunt J, Leibovich S, Richards K (1988) Turbulent shear flows over low hills.  
614 *Quarterly Journal of the Royal Meteorological Society* 114(484):1435–1470  
615
- 616 Hunt JCR, Vilenski GG, Johnson ER (2006) Stratified separated flow around  
617 a mountain with an inversion layer below the mountain top. *Journal of Fluid  
618 Mechanics* 556:105–119  
619
- 620 Hunter JD (2007) Matplotlib: A 2d graphics environment. *Computing in sci-  
621 ence & engineering* 9(03):90–95  
622

- 607 Iversen JD, Rasmussen KR (1999) The effect of wind speed and bed slope on  
608 sand transport. *Sedimentology* 46:723–731
- 609 Jackson PS, Hunt JCR (1975) Turbulent wind flow over a low hill. *Quarterly*  
610 *Journal of the Royal Meteorological Society* 101(430):929–955
- 611 Jiang Q (2014) Applicability of reduced-gravity shallow-water theory to  
612 atmospheric flow over topography. *Journal of the Atmospheric Sciences*  
613 71(4):1460–1479
- 614 Jolivet M, Braucher R, Dovchintseren D, Hocquet S, Schmitt J, ASTER Team  
615 (2021) Erosion around a large-scale topographic high in a semi-arid sedimentary  
616 basin: Interactions between fluvial erosion, aeolian erosion and aeolian  
617 transport. *Geomorphology* 386:107,747
- 618 Kim HG, Patel VC, Lee CM (2000) Numerical simulation of wind flow  
619 over hilly terrain. *Journal of wind engineering and industrial aerodynamics*  
620 87(1):45–60
- 621 Lancaster LNSM J (1984) Climate of the central namib desert. *Madoqua*  
622 1984(1):5–61
- 623 Lancaster N (1985) Winds and sand movements in the namib sand sea. *Earth*  
624 *Surface Processes and Landforms* 10(6):607–619
- 625 Lewis HW, Mobbs SD, Lehning M (2008) Observations of cross-ridge flows  
626 across steep terrain. *Quarterly Journal of the Royal Meteorological Society: A journal of the atmospheric sciences, applied meteorology and physical oceanography* 134(633):801–816
- 627 Liu ZYC, Zimbelman JR (2015) Recent near-surface wind directions inferred  
628 from mapping sand ripples on martian dunes. *Icarus* 261:169–181
- 629 Livingstone I, Warren A (1996) Aeolian geomorphology: an introduction. *Ad-*  
630 *dison Wesley Longman Ltd*
- 631 Livingstone I, Bristow C, Bryant RG, Bullard J, White K, Wiggs GFS, Baas  
632 ACW, Bateman MD, Thomas DSG (2010) The namib sand sea digital  
633 database of aeolian dunes and key forcing variables. *Aeolian Research* 2(2–  
634 3):93–104
- 635 Lorenz R, Claudin P, Andreotti B, Radebaugh J, Tokano T (2010) A 3 km  
636 atmospheric boundary layer on titan indicated by dune spacing and huygens  
637 data. *Icarus* 205(2):719–721
- 638 Lü P, Narteau C, Dong Z, Rozier O, Du Pont SC (2017) Unravelling raked  
639 linear dunes to explain the coexistence of bedforms in complex dunefields.  
Nature communications 8(1):1–9
- 640 Lü P, Narteau C, Dong Z, Claudin P, Rodriguez S, An Z, Fernandez-Cascales  
641 L, Gadal C, Courrech du Pont S (2021) Direct validation of dune instability  
642 theory. *Proceedings of the National Academy of Sciences* 118(17)
- 643 McKee ED (1979) A study of global sand seas, vol 1052. US Government  
644 Printing Office
- 645 Muñoz-Sabater J, Dutra E, Agustí-Panareda A, Albergel C, Arduini G, Bal-  
646 samo G, Boussetta S, Choulga M, Harrigan S, Hersbach H, et al. (2021)  
647 Era5-land: A state-of-the-art global reanalysis dataset for land applications.  
648 Earth System Science Data Discussions pp 1–50

- 652 Pähzt T, Durán O (2020) Unification of aeolian and fluvial sediment transport  
653 rate from granular physics. *Physical review letters* 124(16):168,001
- 654 Pearce KI, Walker IJ (2005) Frequency and magnitude biases in the 'Fryberger'  
655 model, with implications for characterizing geomorphically effective winds.  
656 *Geomorphology* 68(1-2):39–55, DOI 10.1016/j.geomorph.2004.09.030
- 657 Pelletier JD, Field JP (2016) Predicting the roughness length of turbulent flows  
658 over landscapes with multi-scale microtopography. *Earth Surface Dynamics*  
659 4(2):391–405, DOI 10.5194/esurf-4-391-2016
- 660 Rasmussen KR, Iversen JD, Rautaheimo P (1996) Saltation and wind flow  
661 interaction in a variable slope wind tunnel. *Geomorphology* 17:19–28
- 662 Rubin DM, Hunter RE (1987) Bedform alignment in di-  
663 rectinally varying flows. *Science* 237:276–278, DOI  
664 <https://doi.org/10.1126/science.237.4812.276>
- 665 Runyon K, Bridges N, Ayoub F, Newman C, Quade J (2017) An integrated  
666 model for dune morphology and sand fluxes on mars. *Earth and Planetary  
667 Science Letters* 457:204–212
- 668 Seidel DJ, Zhang Y, Beljaars A, Golaz JC, Jacobson AR, Medeiros B (2012)  
669 Climatology of the planetary boundary layer over the continental united  
670 states and europe. *Journal of Geophysical Research: Atmospheres* 117(D17)
- 671 Shao Y (2008) Physics and modelling of wind erosion, vol 37. Springer Science  
672 & Business Media
- 673 Shen Y, Zhang C, Huang X, Wang X, Cen S (2019) The effect of wind speed  
674 averaging time on sand transport estimates. *Catena* 175:286–293
- 675 Sheridan PF, Vosper SB (2006) A flow regime diagram for forecasting lee  
676 waves, rotors and downslope winds. *Meteorological Applications* 13(2):179–  
677 195
- 678 Sherman DJ, Farrell EJ (2008) Aerodynamic roughness lengths over movable  
679 beds: Comparison of wind tunnel and field data. *Journal of Geophysical  
680 Research: Earth Surface* 113(2):1–10, DOI 10.1029/2007JF000784
- 681 Sherman DJ, Li B (2012) Predicting aeolian sand transport rates: A reevalu-  
682 ation of models. *Aeolian Research* 3(4):371–378
- 683 Smith AB, Jackson DWT, Cooper JAG (2017) Three-dimensional airflow and  
684 sediment transport patterns over barchan dunes. *Geomorphology* 278:28–42
- 685 Song Q, Gao X, Lei J, Li S (2019) Spatial distribution of sand dunes and their  
686 relationship with fluvial systems on the southern margin of the taklimakan  
687 desert, china. *Geomatics, Natural Hazards and Risk* 10(1):2408–2428
- 688 Spalding DB (1961) A single formula for the "law of the wall"
- 689 Stull R (2006) 9 - the atmospheric boundary layer. In: Wallace JM, Hobbs  
690 PV (eds) *Atmospheric Science* (Second Edition), second edition edn, Aca-  
691 demic Press, San Diego, pp 375–417, DOI <https://doi.org/10.1016/B978-0-12-732951-2.50014-4>
- 693 Stull RB (1988) An introduction to boundary layer meteorology, vol 13.  
694 Springer Science & Business Media
- 695 Sullivan PP, McWilliams JC (2010) Dynamics of winds and currents coupled  
696 to surface waves. *Annual Review of Fluid Mechanics* 42:19–42

- 697 Sykes RI (1980) An asymptotic theory of incompressible turbulent boundary-  
698 layer flow over a small hump. *Journal of Fluid Mechanics* 101(3):647–670  
699 Ungar JE, Haff PK (1987) Steady state saltation in air. *Sedimentology* 34:289–  
700 299  
701 Unsworth C, Parsons D, Hardy R, Reesink A, Best J, Ashworth P, Keevil G  
702 (2018) The impact of nonequilibrium flow on the structure of turbulence  
703 over river dunes. *Water Resources Research* 54(9):6566–6584  
704 Uppala SM, Källberg P, Simmons AJ, Andrae U, Bechtold VDC, Fiorino M,  
705 Gibson J, Haseler J, Hernandez A, Kelly G, et al. (2005) The era-40 re-  
706 analysis. *Quarterly Journal of the Royal Meteorological Society: A journal*  
707 of the atmospheric sciences, applied meteorology and physical oceanography  
708 131(612):2961–3012  
709 Virtanen P, Gommers R, Oliphant TE, Haberland M, Reddy T, Cournapeau  
710 D, Burovski E, Peterson P, Weckesser W, Bright J, et al. (2020) Scipy 1.0:  
711 fundamental algorithms for scientific computing in python. *Nature methods*  
712 17(3):261–272  
713 Vosper SB (2004) Inversion effects on mountain lee waves. *Quarterly Journal*  
714 of the Royal Meteorological Society: A journal of the atmospheric sciences,  
715 applied meteorology and physical oceanography 130(600):1723–1748  
716 Walker IJ, Shugar DH (2013) Secondary flow deflection in the lee of transverse  
717 dunes with implications for dune morphodynamics and migration. *Earth*  
718 surface processes and landforms 38(14):1642–1654  
719 Walker IJ, Hesp PA, Davidson-Arnott RG, Bauer BO, Namikas SL,  
720 Ollerhead J (2009) Responses of three-dimensional flow to variations  
721 in the angle of incident wind and profile form of dunes: Greenwich  
722 dunes, prince edward island, canada. *Geomorphology* 105:127–138, DOI  
723 10.1016/j.geomorph.2007.12.019  
724 Zhang C, Li Q, Zhou N, Zhang J, Kang L, Shen Y, Jia W (2016) Field obser-  
725 vations of wind profiles and sand fluxes above the windward slope of a sand  
726 dune before and after the establishment of semi-buried straw checkerboard  
727 barriers. *Aeolian Research* 20:59–70, DOI 10.1016/j.aeolia.2015.11.003  
728 Zilker DP, Hanratty TJ (1979) Influence of the amplitude of a solid wavy wall  
729 on a turbulent flow. part 2. separated flows. *Journal of Fluid Mechanics*  
730 90(2):257–271  
731 Zilker DP, Cook GW, Hanratty TJ (1977) Influence of the amplitude of a solid  
732 wavy wall on a turbulent flow. part 1. non-separated flows. *Journal of Fluid*  
733 *Mechanics* 82(1):29–51

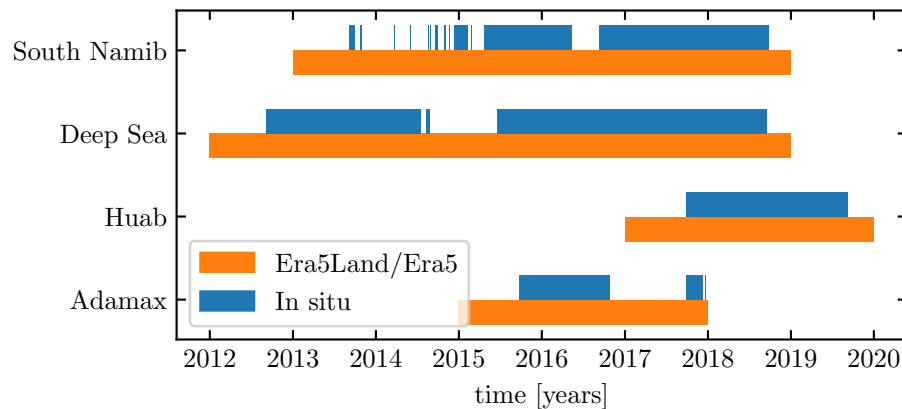


**Fig. S1** Gant chart representing the valid time steps for the two data sets, for all stations.

734     **Supplementary Material for *Boundary-Layer Meteorology* Sample  
735     Paper: Instructions for Authors**

736     **First Author\* · Second Author · Third Author**

737  
738     \*Affiliation and email address for the corresponding author only (note that  
739     the corresponding author does not need to be the first author).

740     **1. Shear velocity and calibration of the hydrodynamical roughness**

741     As the regionally predicted and locally measured velocities are available at  
742     different heights, we can not compare them directly. We then convert all  
743     velocities into shear velocities  $u_*$ , characteristic of the turbulent velocity profile  
744     (Spalding 1961; Stull 1988):

$$\frac{u(z)}{u_*} = \frac{1}{\kappa} \ln \left( \frac{z}{z_0} \right), \quad (16)$$

745     where  $z$  is the vertical coordinate,  $\kappa \approx 0.4$  the von Kármán constant and  $z_0$   
746     the hydrodynamic roughness. Several field measurements of hydrodynamic  
747     roughnesses are available. In the absence of sediment transport, it scales with  
748     the geometric roughness of the topography (Pelletier and Field 2016). When  
749     transport occurs, it then scales with the thickness of the transport layer  
750     ( $\sim 1$  mm), depending on the wind velocity and grain properties (Sherman and Farrell 2008; Zhang et al. 2016; Field and P

751     ~  
752     The different environments of our stations (vegetated, arid, sandy) makes  
753     it difficult to develop a precise model for the computation of the hydrodynamic  
754     roughness. Furthermore, we do not have precise enough topographical measurements  
755     that would allow to compute the geometric roughness. We choose to leave  
756     aside this complexity, and use a different approach. The selected hydrodynamic

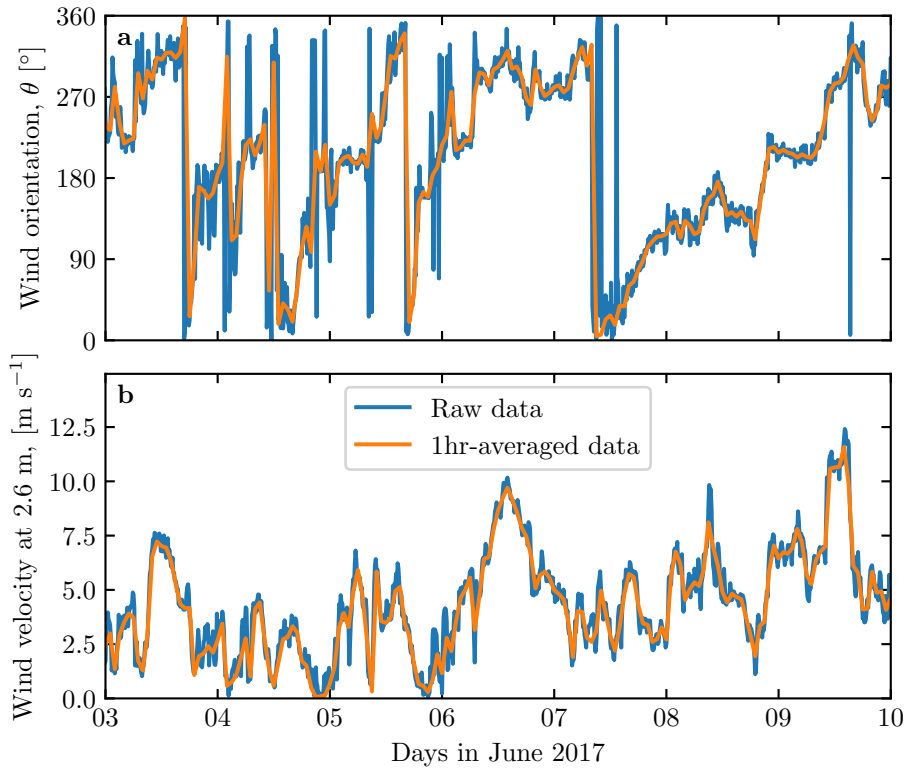


**Fig. S2** Comparison between raw local wind measurements, and centered averaged data over one hour for the South Namib station. **a:** wind direction. **b:** wind velocity at the measurement height, 2.6 m.

roughness is then the one that leads to the best possible matching between the regionally predicted and locally measured winds.

For each station, the hydrodynamic roughness is calibrated by finding the one that minimizes the relative difference  $\delta$  between the wind vectors of both datasets:

$$\delta = \frac{\sqrt{\langle \|\mathbf{u}_{*,\text{era}} - \mathbf{u}_{*,\text{station}}\|^2 \rangle_t}}{\sqrt{\langle \|\mathbf{u}_{*,\text{era}}\| \rangle_t \langle \|\mathbf{u}_{*,\text{station}}\| \rangle_t}} \quad (17)$$

This  $\delta$ -parameter is computed for hydrodynamic roughness values ranging from  $10^{-5}$  m to  $10^{-2}$  m for the different stations. Note that for the Deep Sea and South Namib stations, where the giant dunes feedback presumably affect the wind, we take into account the non-deflected winds only in the calculation of  $\delta$  (with a  $15^\circ$  tolerance).

A shown by figure S3, the minimum of  $\delta$  in the space ( $z_0, \text{Era}, z_0, \text{in situ}$ ,  $z_0^{\text{Era5Land}}$ ,  $z_0^{\text{local}}$ ) forms a line. We thus take the roughness of the Era5Land dataset as the typical value when sediment transport occurs,  $10^{-3}$  m, corresponding to the thickness of the transport layer (Durán et al. 2011). It leads for

771 the Adamax, Deep Sea, Huab and South Namib stations values of 2.7 mm,  
 772 0.76 mm, 0.12 mm and 0.48 mm, respectively.

773 The choice of the hydrodynamic roughness values ~~only~~ impacts the calcu-  
 774 lated shear velocities, ~~but note only, but not~~ the wind directions. As such, most  
 775 of our conclusions are ~~then~~ independent of such a choice, ~~and only~~. However, it  
 776 ~~may affect~~ the magnitude of the wind velocity attenuation ~~in confined situation~~  
 777 ~~might be affected/amplification in flow confinement situations~~.

## 778 2. Extraction of the ABL properties

779 ~~In order to estimate the relevant~~ The estimation of the non-dimensional num-  
 780 bers, ~~one need to estimate in addition to the wind and dune properties~~ some parameters of the ABL requires the computation of meteorological  
 781 quantities representative of the current atmospheric boundary layer. In arid  
 782 areas, the vertical structure of the atmosphere can be approximated by well  
 783 mixed convective boundary layer of height  $H$ , topped by the stratified free  
 784 atmosphere (Stull 1988; Shao 2008). In this type of structure, the virtual potential  
 785 temperature is constant inside the boundary layer, and then increases linearly  
 786 in the stratified free atmosphere (Fig. S9a):

$$T_{vp}(z) = \begin{cases} T_0 & \text{for } z < H, \\ T_0 \left( 1 + \frac{\Delta T_{vp}}{T_0} + \frac{N^2}{g} (z - H) \right) & \text{for } z > H, \end{cases} \quad (18)$$

788 where,  $T_0$  is the surface virtual potential temperature,  $\Delta T_{vp}$  the discontinuity  
 789 at the capping layer and  $N$  the Brunt-Väisälä frequency, characteristic of the  
 790 stratification.

791 The Era5 dataset provides a direct ~~bulk~~-estimate of the ABL depth  $H$   
 792 from a bulk Richardson number calculation, as well as vertical profiles of the  
 793 geopotential  $\phi$ , temperature  $T$  and specific humidity  $e_w$  at given pressure levels  
 794  $P$ . From these quantities, the virtual potential temperature ~~, which takes into~~  
 795 ~~account the vertical pressure and humidity changes~~, can be calculated as:

$$T_{vp} = T (1 + [R_M - 1] e_w) \left( \frac{P_0}{P} \right)^{P_c(1-0.24e_w)}, \quad (19)$$

796 where  $P_0 = 10^5$  Pa is the standard pressure,  $P_c = 0.2854$  the Poisson coefficient  
 797 for dry air and  $R_M = 1.61$  is the ratio between the ~~molecular~~ molecular masses  
 798 of dry air and water. The vertical coordinates are calculated as:

$$z = \frac{\phi R_t}{g R_t - \phi}, \quad (20)$$

799 where  $R_t = 6356766$  m is the average Earth radius, and  $g = 9.81$  m s<sup>-2</sup> the  
 800 gravitational acceleration.

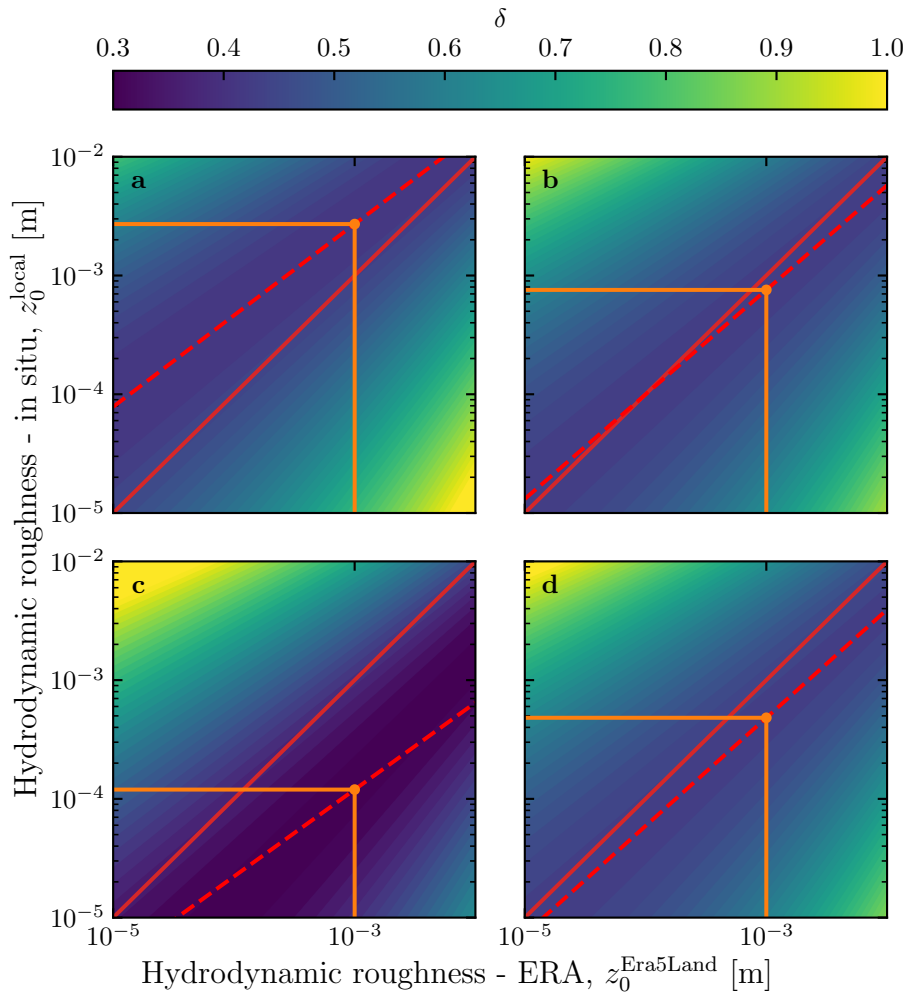


**Fig. S3** Calibration of the hydrodynamic roughnesses. The metric  $\delta$  defined in (17) is represented in colorscale as a function of the hydrodynamic roughnesses chosen for the Era5-Land and in situ datasetslocal winds, for the Adamax-(a) Adamax, Deep Sea-(b) Deep Sea, Huab-(c) Huab and South Namib-(d) StationsSouth Namib stations. The red dashed and plain lines shows the minima of  $\delta$  and the identity line, respectively. The orange lines and dots highlight the chosen hydrodynamic roughnesses for the local datasetswinds, by imposing  $z_0^{\text{ERA}} = 1 \text{ mm}$ , leading  $z_0^{\text{Era5Land}} = 1 \text{ mm}$ . It leads for each station to 2.7 mm, 0.76 mm, 0.12 mm and 0.48 mm, respectively.

801 Example of obtained vertical profiles of the virtual potential temperature  
 802 are shown in Fig. S9a. On each of them, an average is computed below the  
 803 ABL depth directly given by the Era5 dataset, and a linear function is fitted  
 804 above.

805 Note that under the Boussinesq approximation, the temperature  
 806 variations are assumed to induce most of those of the density, leading to

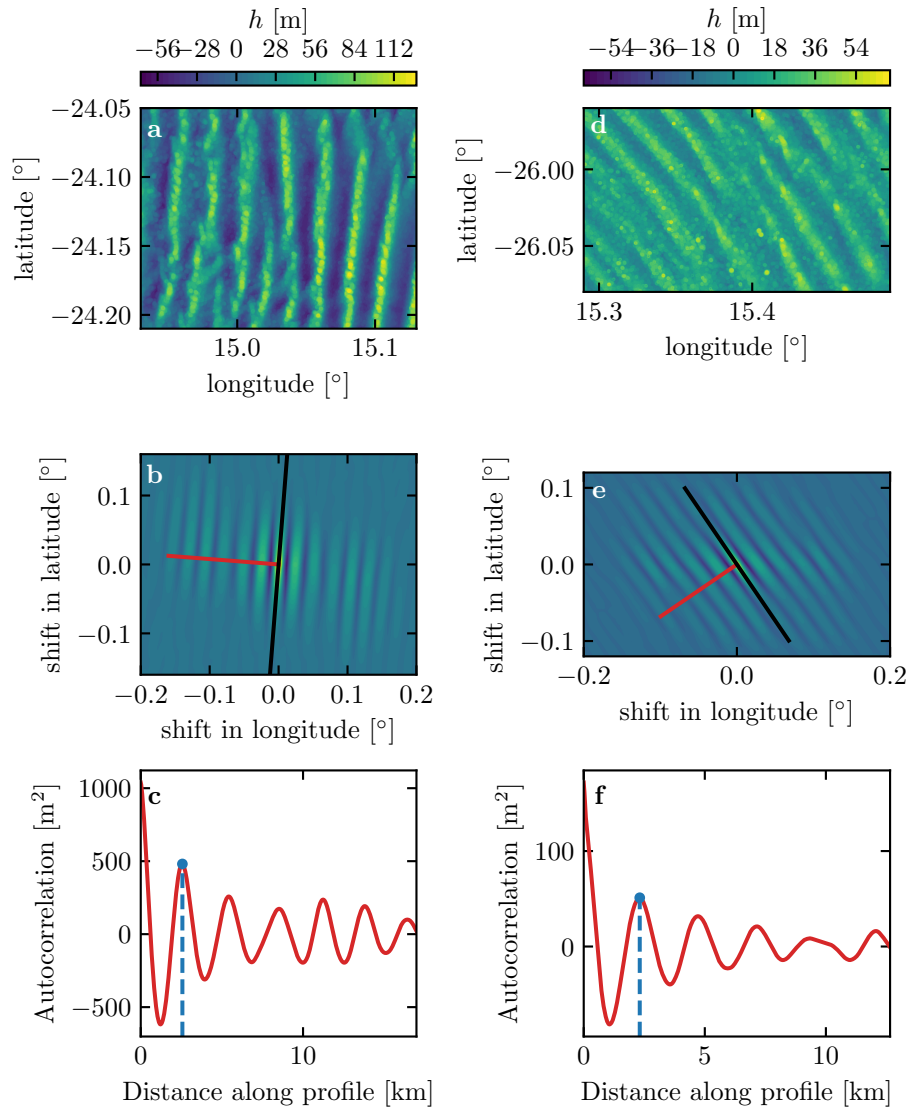


**Fig. S4** Analysis of the DEMs of the Deep Sea (left column – **a**, **b**, **c**) and South Namib (right column – **d**, **e**, **f**) stations. **a–d**: Detrended topography (a second order polynomial is first fitted and then removed). **b–e**: autocorrelation matrix shown in colorscale. The black line shows the detected orientation, and the red line the profile along which the wavelength is calculated, shown in **c–f**. The blue lines and dots show the first peak of the autocorrelation profile, whose abscissa gives the characteristic wavelength of the dune pattern.

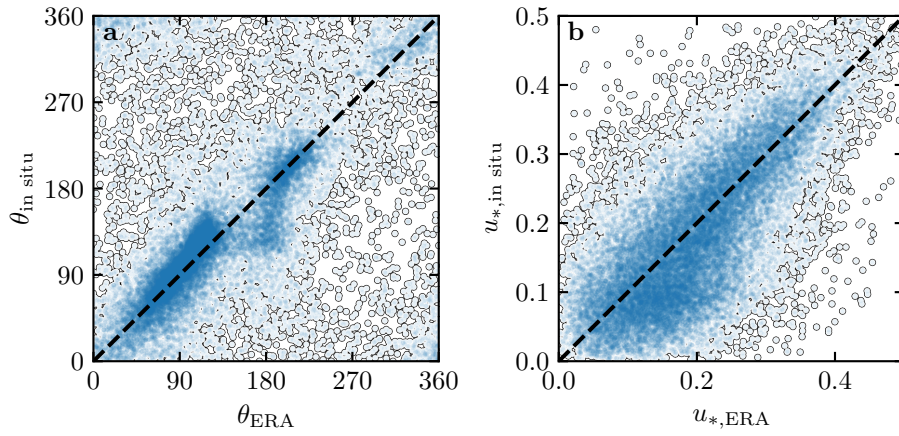


**Fig. S5** Statistical agreement of the wind orientation (a) and velocity (b) between the Era5Land dataset and the local measurements for the Huab and Adamax stations. Note how the points are clustered around identity lines (dashed and black).

807  $\Delta\rho/\rho \simeq \Delta T_{\text{vp}}/T_{\text{vp}}$ . Here,  $T_{\text{vp}}/T_{\text{vp}}$  is the relative virtual potential temperature  
 808 jump at the capping, directly measured on the vertical profiles.

809 Following ?, the relative density jump at the capping layer  $\Delta\rho/\rho_0 \simeq \Delta T_{\text{vp}}/T_0$   
 810 (see supplementary material of (Andreotti et al. 2009)). Note that we removed  
 811 some profiles that displayed a vertical structure that could not be approximated  
 812 by the simple model used here, leading for example to negative values of  $\Delta T_{\text{vp}}$   
 813 (see Fig. S9b). While these profiles dominantly occurs in winter, when the two  
 814 winds blows, they are evenly spread across the hours of the day, and represent  
 815 12 % of our data only (see Fig. S9c-d). For these reasons, we are confident  
 816 this does not affect pour conclusions.

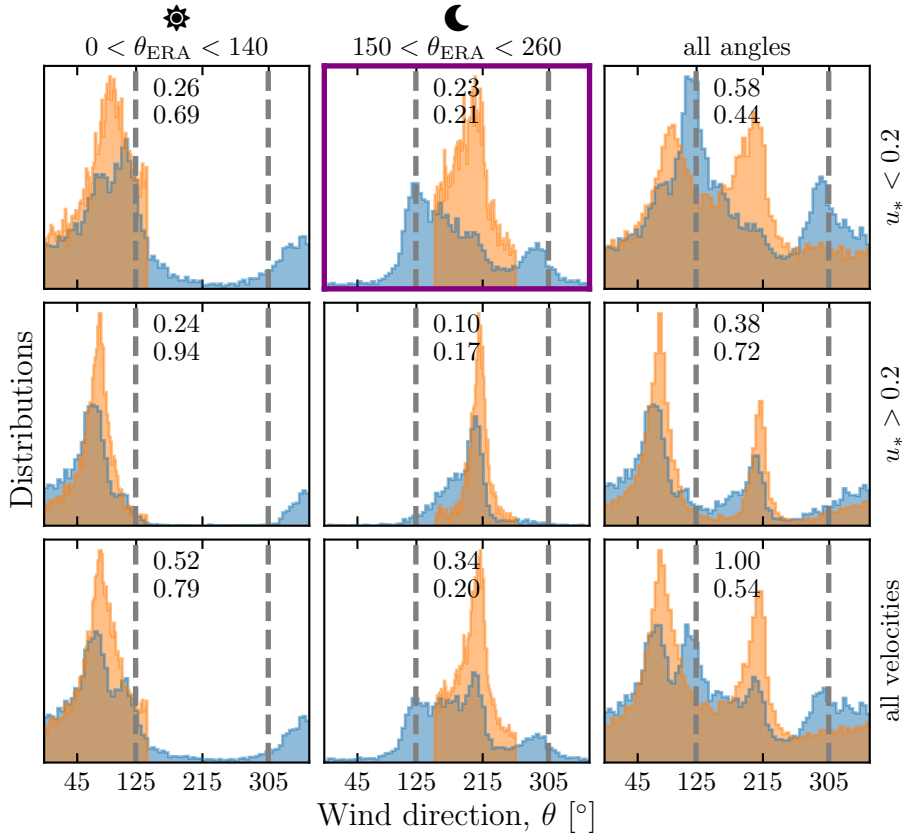


**Fig. S6** Distributions of wind direction at the South Namib Station for the Era5Land climate reanalysis (orange) and the [in-situ local](#) measurements (blue). In each subplot, both distributions are plotted from the same time steps, selected with constraints on the wind direction (columns) and/or wind velocity (rows) in the Era5Land dataset. The [grey dashed gray vertical dashed](#) lines indicate the dune orientation. The [numbers at the top center give the percentage of time steps selected in each sub-range, as well as the percentage of them corresponding to the day between 1000 UTC and 2200 UTC](#). The purple frame highlights the regime (small wind velocities, nocturnal summer wind) during which the wind data from both datasets differs. A similar figure can be obtained for the South Namib station (see Fig. 3).

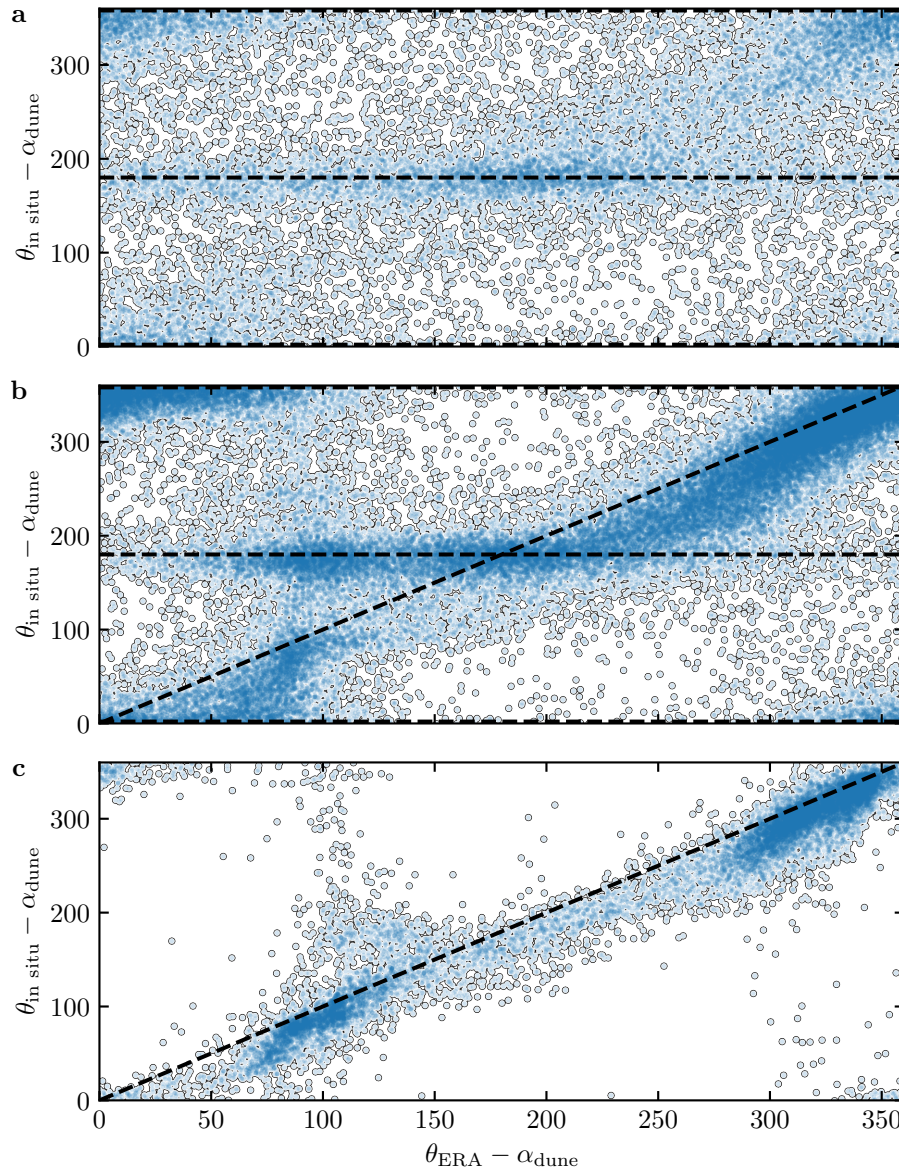


**Fig. S7** Statistical comparison of the wind orientation between the Era5Land dataset and the local measurements for the South Namib and Deep Sea stations, for different velocity ranges. **a:**  $u_{*,\text{ERA}} < 0.1 \text{ m s}^{-1}$ . **b:**  $0.1 < u_{*,\text{ERA}} \leq 0.25 \text{ m s}^{-1}$ . **c:**  $u_{*,\text{ERA}} \geq 0.25 \text{ m s}^{-1}$ . Note that the measured dune orientations are subtracted to the wind orientation, which allows to plot both stations on the same graph. Black dashed lines indicate locally measured orientations aligned with the dune crests (here 0°, 180° and 360° – **a, b**), as well as the identity lines (**b, c**).

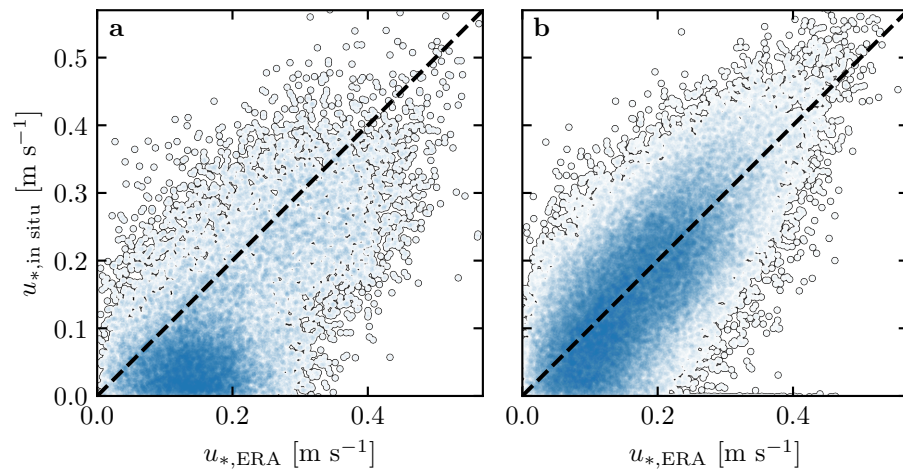


**Fig. S8** Statistical comparison of the wind velocity between the Era5Land dataset and the local measurements for the South Namib and Deep Sea stations. **a:** Nocturnal summer easterly wind. **b:** Diurnal southerly wind. Black dashed lines are identity lines. The angle ranges used to select diurnal and nocturnal summer winds are those taken in Fig. 3 and Fig. S6.

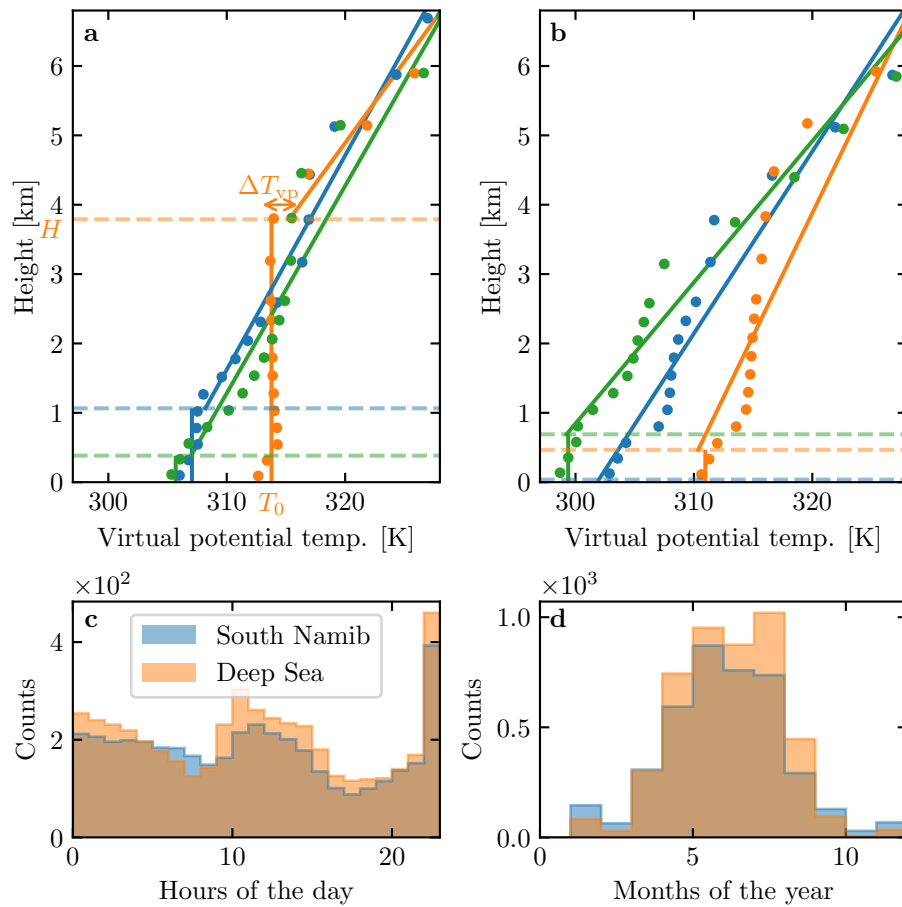


**Fig. S9** **a:** Vertical profiles of the virtual potential temperature at 3 different time steps (blue - 29/11/2012 - 1100 UTC, orange - 21/03/2017 - 1200 UTC, green - 21/03/2017 - 2000 UTC) at the South Namib station. Dots: data from the ERA5 reanalysis. Transparent dashed lines: boundary layer height given by the ERA5 reanalysis, calculated from the bulk Richardson number (Seidel et al. 2012). Plain lines: vertical ([boundary\\_layerABL](#)) and linear ([free\\_atmosphereFA](#)) fits to estimate the quantities in Fig. S10. **b:** Examples of ill-processed vertical profiles at 3 different time steps (blue - 2/12/2013 - 2300 UTC, orange - 20/03/2017 - 0000 UTC, green - 14/07/2017 - 1400 UTC) at the South Namib station. **c:** Hourly distribution of ill-processed vertical profiles. **d:** Monthly distribution of ill-processed vertical profiles. These profiles are ill-processed because the temperature found at the boundary layer from the linear fit in the free-atm is smaller than the temperature found at the top of the boundary layer from the vertical fit.

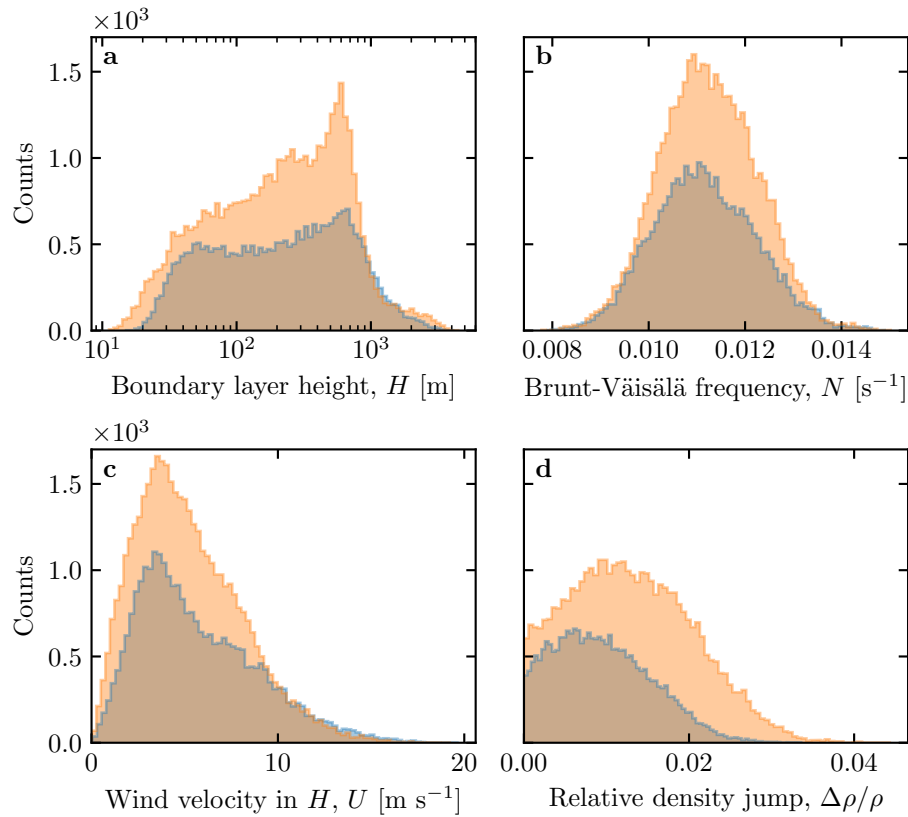


**Fig. S10** Distributions of the meteorological parameters resulting from the processing of the Era5-Land data for the South Namib (blue) and the Deep Sea (orange) stations.

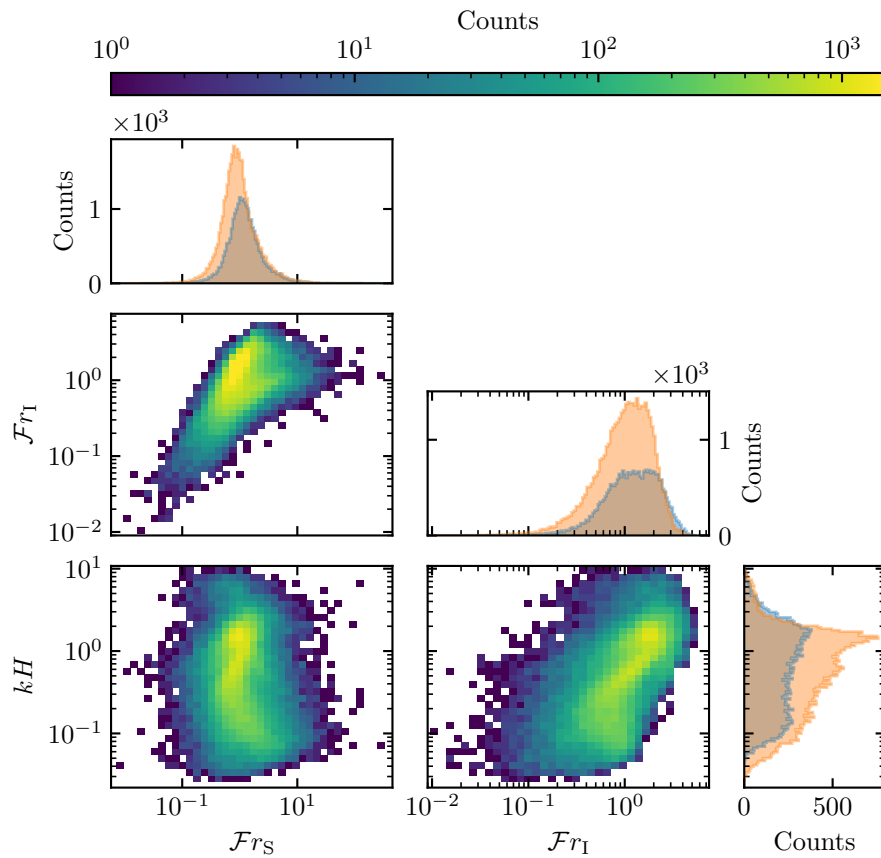


**Fig. S11** Non-dimensional parameters distributions. For the marginal distributions, the orange correspond to the South Namib station, and the blue to the Deep Sea station.

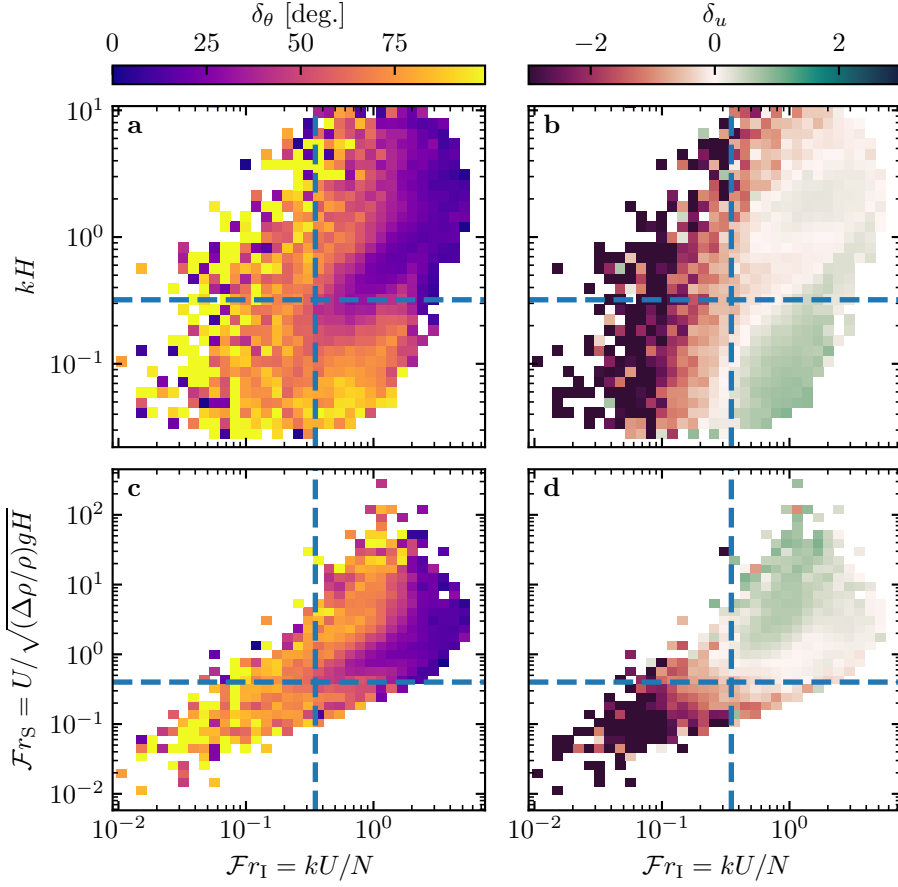


**Fig. S12** Regime diagrams of the wind deviation  $\delta_\theta$  and relative attenuation/amplification  $\delta_u$  in the spaces  $(\mathcal{Fr}_I, kH)$  ( $\mathcal{F}_I, kH$ ) and  $(\mathcal{Fr}_I, \mathcal{Fr}_S)(\mathcal{F}_I, \mathcal{F})$ , containing the data from both the Deep Sea and South Namib stations. Blue dashed lines empirically delimit the different regimes. The point density in each bin of the diagrams is shown in Fig. S11. The regime diagrams in the space  $(\mathcal{Fr}_S, kH)$  ( $\mathcal{F}_S, kH$ ) are shown in Fig. 5 of the main article.

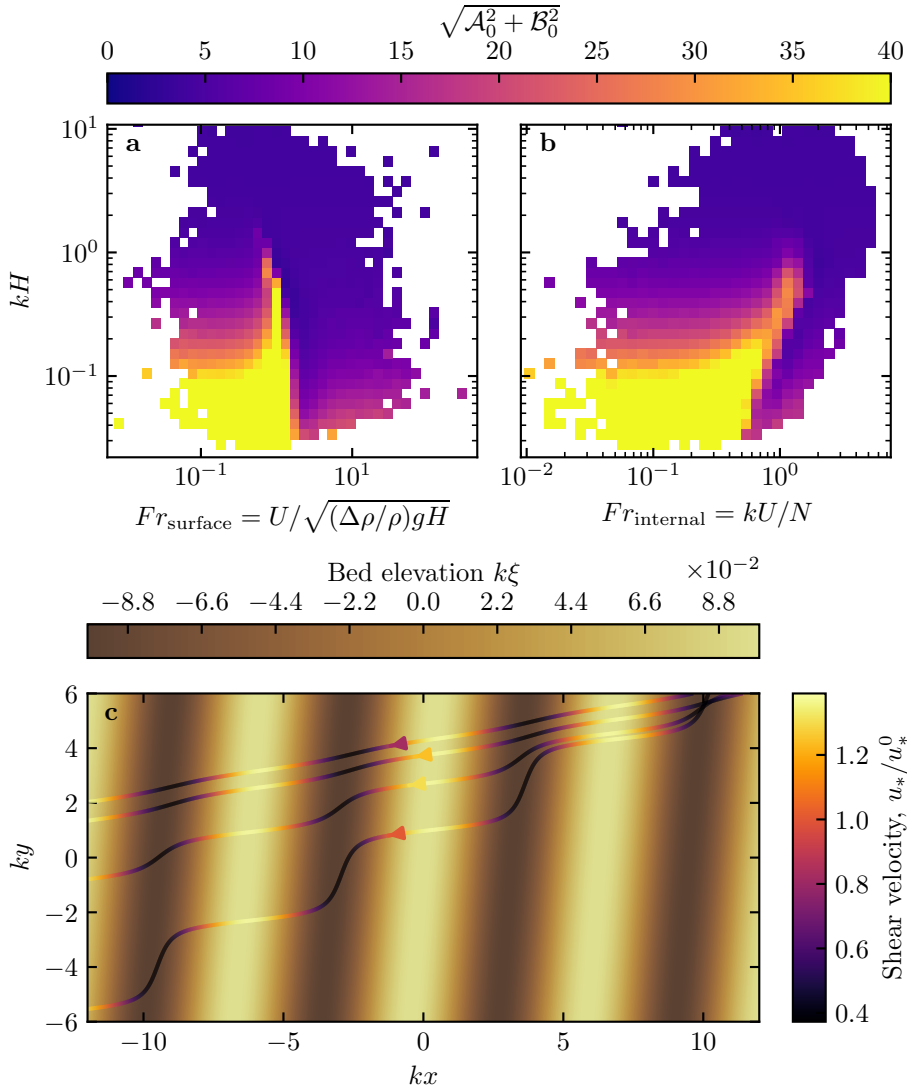


**Fig. S13** Physical interpretation of the flow disturbance. (a) and (b) Magnitude of the disturbance induced by a sinusoidal topography calculated from the time series of the non-dimensional numbers presented in Figures 4 and 5 using the linear model of Andreotti et al. (2009). (c) Shear velocity streamlines represented in the case of the Deep Sea station, for increasing values of  $\sqrt{\mathcal{A}_0^2 + \mathcal{B}_0^2}$ . From the upper to the lower streamline, values of  $(kH, Fr_{\text{surface}}, Fr_{\text{internal}}, \mathcal{A}_0, \mathcal{B}_0, \sqrt{\mathcal{A}_0^2 + \mathcal{B}_0^2})$  are  $(1.9, 0.6, 1.5, 3.4, 1.0, 3.5)$ ,  $(1.5, 0.3, 0.4, 4.8, 1.4, 5.0)$ ,  $(0.1, 3.5, 1.0, 8.6, 0.1, 8.6)$ ,  $(0.5, 0.05, 0.04, 9.6, 2.5, 9.9)$ .